Monthly Notices
of the
ROYAL ASTRONOMICAL SOCIETY

MNRAS **449,** 2883–2900 (2015) doi:10.1093/mnras/stv372

The nature of the [C II] emission in dusty star-forming galaxies from the SPT survey

B. Gullberg,[1⋆] C. De Breuck,[1] J. D. Vieira,[2] A. Weiß,[3] J. E. Aguirre,[4] M. Aravena,[5,6] M. Béthermin,[1] C. M. Bradford,[7] M. S. Bothwell,[8] J. E. Carlstrom,[9,10,11,12] S. C. Chapman,[13] C. D. Fassnacht,[14] A. H. Gonzalez,[15] T. R. Greve,[16] Y. Hezaveh,[17] W. L. Holzapfel,[18] K. Husband,[19] J. Ma,[15] M. Malkan,[20] D. P. Marrone,[21] K. Menten,[3] E. J. Murphy,[22] C. L. Reichardt,[18] J. S. Spilker,[21] A. A. Stark,[23] M. Strandet[3] and N. Welikala[24]

Affiliations are listed at the end of the paper

Accepted 2015 February 19. Received 2015 January 27; in original form 2014 September 11

ABSTRACT

We present [C II] observations of 20 strongly lensed dusty star-forming galaxies at $2.1 < z < 5.7$ using Atacama Pathfinder EXperiment and *Herschel*. The sources were selected on their 1.4 mm flux ($S_{1.4\,\mathrm{mm}} > 20$ mJy) from the South Pole Telescope (SPT) survey, with far-infrared (FIR) luminosities determined from extensive photometric data. The [C II] line is robustly detected in 17 sources, all but one being spectrally resolved. 11 out of 20 sources observed in [C II] also have low-*J* CO detections from Australia Telescope Compact Array. A comparison with mid- and high-*J* CO lines from Atacama Large Millimeter/submillimeter Array reveals consistent [C II] and CO velocity profiles, suggesting that there is little differential lensing between these species. The [C II], low-*J* CO and FIR data allow us to constrain the properties of the interstellar medium. We find [C II] to CO(1–0) luminosity ratios in the SPT sample of 5200 ± 1800, with significantly less scatter than in other samples. This line ratio can be best described by a medium of [C II] and CO emitting gas with a higher [C II] than CO excitation temperature, high CO optical depth $\tau_{\mathrm{CO(1-0)}} \gg 1$, and low to moderate [C II] optical depth $\tau_{\mathrm{[C\,II]}} \lesssim 1$. The geometric structure of photodissociation regions allows for such conditions.

Key words: galaxies: high-redshift – galaxies: ISM – galaxies: starburst – infrared: galaxies – submillimetre: galaxies.

1 INTRODUCTION

The discovery of (sub)millimeter-selected dusty star-forming galaxies (DSFGs) at high redshifts (e.g. Smail, Ivison & Blain 1997; Barger et al. 1998; Hughes et al. 1998) fundamentally changed our view of galaxy formation and evolution. DSFGs are massive ($M_\star \sim 10^{11}$ M$_\odot$; e.g. Hainline et al. 2011; Michałowski et al. 2012) and gas-rich ($M_{\mathrm{gas}} \sim 3$–5×10^{10} M$_\odot$; e.g. Greve et al. 2005; Tacconi et al. 2010; Bothwell et al. 2013a), and have star formation rates $\gtrsim 1000$ M$_\odot$yr^{-1} (e.g. Chapman et al. 2005). The properties of these galaxies remain a challenge for conventional galaxy formation models (e.g. Baugh et al. 2005; Lacey et al. 2010; Benson 2012; Hayward et al. 2013).

Thanks to the availability of new space- and ground-based submillimetre facilities, our knowledge of the interstellar medium (ISM) in massive gas-rich galaxies at high redshift has dramatically improved in the past decade (Solomon & Vanden Bout 2005; Carilli & Walter 2013; Casey, Narayanan & Cooray 2014). The most commonly used lines for studying the ISM in DSFGs at high redshift are the rotational transitions of carbon monoxide (CO) and the [C II] $\lambda 158$ μm fine structure line. The latter is the most important cooling line in the ISM (Dalgarno & McCray 1972), and traces neutral gas exposed to ultraviolet photons from young stars. The [C II] line can therefore be used to probe the stellar radiation field and how it affects the physical conditions of the gas. The bulk of the [C II] emission line (70 per cent in Stacey et al. 1991a, 2010) is believed to originate from photodissociation regions (PDRs), and the remainder from X-ray-dominated regions (XDRs), cosmic-ray-dominated regions (CRDRs), ionized regions (H II regions; Meijerink, Spaans & Israel 2007), low-density warm gas and/or diffuse HI clouds (Madden et al. 1997).

The [C II] fine structure transition ($\nu_{\mathrm{rest}}^{\mathrm{[C\,II]}} = 1900.54$ GHz) is nearly unobservable from the ground at $z < 1$ due to strong

⋆E-mail: bgullber@eso.org

atmospheric absorption. The only low-z [C II] samples have been observed with airborne (Crawford et al. 1986; Stacey et al. 1991a) or space-based observatories (Malhotra et al. 2001; Brauher, Dale & Helou 2008; Díaz-Santos et al. 2013; Farrah et al. 2013; De Looze et al. 2014; Sargsyan et al. 2014). Submillimetre atmospheric windows provide some access to the line from the ground at $z > 1$, with atmospheric transparency continuing to improve towards higher redshifts (longer wavelengths). As a consequence, the first high-z [C II] detection was reported for the $z = 6.42$ quasar host galaxy SDSSJ1148+5251 a decade ago (Maiolino et al. 2005). The number of [C II] detections has been steadily increasing since then, thanks to facilities such as the Caltech Submillimeter Observatory (CSO), the Submillimeter Array, the IRAM[1] Plateau de Bure Interferometer, the Atacama Pathfinder EXperiment (APEX), the *Herschel Space Observatory*, the Combined Array for Research in Millimeter-wave Astronomy, and the Atacama Large Millimeter/submillimeter Array (ALMA). At $1 < z < 2$, 21 [C II] detections were made using the redshift (z) and Early Universe Spectrometer (ZEUS) on CSO (Hailey-Dunsheath et al. 2010; Stacey et al. 2010; Brisbin et al. 2015), while *Herchel* detected three [C II] lines at $1.5 < z < 3$ (Ivison et al. 2010; Valtchanov et al. 2011; George et al. 2013). 17 have been added to the number of $z > 4$ [C II] detections in the past decade (Maiolino et al. 2005, 2009; Iono et al. 2006; Ivison et al. 2010; Wagg et al. 2010; Cox et al. 2011; De Breuck et al. 2011; Swinbank et al. 2012; Venemans et al. 2012; Walter et al. 2012; Riechers et al. 2013; Wang et al. 2013; De Breuck et al. 2014; Neri et al. 2014; Rawle et al. 2014). Many of these objects have been selected based on the presence of a luminous active galactic nuclei (AGN; e.g. Maiolino et al. 2005; Stacey et al. 2010; Wang et al. 2013), while others have been selected as starburst galaxies (e.g. Ivison et al. 2010; Hailey-Dunsheath et al. 2010; Stacey et al. 2010; Cox et al. 2011; Swinbank et al. 2012; Walter et al. 2012; Riechers et al. 2013; Brisbin et al. 2015). This leads to a heterogeneous sample of high-z [C II] detections, containing a mixture of AGN and starburst-dominated systems. The heterogeneity of the sample complicates the interpretation of trends within it. Stacey et al. (2010) suggest, based on the [C II]/FIR and [C II] to CO(1–0) luminosity ratios, that [C II] emission originates mainly from PDRs and that the ISM and stellar radiation field in these $z \sim 1$–2 galaxies resemble that observed for local starburst systems. These studies have followed the conclusion of Crawford et al. (1985) that the [C II] emission is optically thin or reaching unity opacity ($\tau \lesssim 1$); however, this was recently challenged by Neri et al. (2014), who argued for optically thick [C II].

Here, we present [C II] observations of 20 gravitationally lensed DSFGs in the redshift range $z \sim 2.1$–5.7 discovered by the South Pole Telescope (SPT; Vieira et al. 2010; Carlstrom et al. 2011). These 20 sources are a subset of those selected from the first 1300 deg^2 of the 2500 deg^2 SPT-SZ survey. Follow-up observations with ALMA have provided spectroscopic redshifts for all of these objects (Vieira et al. 2013; Weiß et al. 2013). We also include two new sources observed in Cycle 1 (see Appendix A for details). The bright ($S_{1.4\mathrm{mm}} > 20$ mJy) flux selection of the SPT sample ensures that virtually all sources will be gravitationally magnified, with a bias towards $z > 2$ (Hezaveh & Holder 2011; Weiß et al. 2013). The magnified emission allows us to study the ISM in these DSFGs in greater detail, using fine structure and molecular lines such as [C II] and CO. By including low-J CO observations for 11 sources in our analysis, we determine the physical state of the ISM by studying the [C II] and CO(1–0) line intensity ratios.

This paper is organized as follows: in Section 2, we describe the [C II] and CO observations, and the results for these observations are given in Section 3. In Section 4, we present our analysis, and discuss the implications in Section 5. Our conclusions and summary are given in Section 6. Throughout this paper, we adopt the cosmology: $H_0 = 71$ km s^{-1} Mpc^{-1}, $\Omega_\Lambda = 0.73$, and $\Omega_\mathrm{m} = 0.27$ (Komatsu et al. 2011).

2 OBSERVATIONS

2.1 Supporting ALMA and ATCA observations

The 20 DSFGs presented here are a subset of 100 strongly lensed DSFGs selected over the 2500 deg^2 SPT-SZ survey. See table 1 in Weiß et al. (2013) and Table A1 in Appendix A for the full names and positions. Mid- and high-J CO rotational lines (i.e. CO(3–2), CO(4–3), CO(5–4) and/or CO(6–5)) were detected for 23[2] DSFGs with the ALMA. The redshifts of all our [C II] targets are determined by one or more CO lines plus the [C II] line itself and are therefore robust.

In addition, low-J CO emission lines (CO(1–0) or CO(2–1)) were observed with the Australia Telescope Compact Array (ATCA) for 11 of the SPT DSFGs for which [C II] observations are presented in this paper (Aravena et al. 2013; Aravena et al., in preparation). Absolute flux calibration of the ATCA data is estimated to be accurate to within 15 per cent. Details of the observations, fluxes, and associated uncertainties will be presented in a forthcoming paper by Aravena et al.

2.2 APEX/FLASH

We targeted all galaxies in the SPT DSFG sample with known redshifts that place the [C II] line at frequencies which are observable with good atmospheric transparency using the First Light APEX Submillimetre Heterodyne receiver (FLASH; Heyminck et al. 2006). 11 sources at $4.2 < z < 5.7$ were observed in the 345 GHz channel between 2012 August and 2014 June, and six sources at $3.1 < z < 3.8$ were observed with the 460 GHz channel between 2013 March and August during Max Planck time. All observations were done in good weather conditions with an average precipitable water vapour <1.0 mm, yielding typical system temperatures of 230 and 170 K for the 345 and 460 GHz observations, respectively. The beam sizes/antenna gains are 22.0 arcsec/40 Jy K^{-1} and 13.5 arcsec/48 Jy K^{-1} for the lowest and highest observed frequencies of the [C II] line, respectively. The beam size is much larger than the observed Einstein radii of these sources and thus they are unresolved (Hezaveh et al. 2013; Vieira et al. 2013). The 82 h of observations were done in wobbler switching mode, with switching frequency of 1.5 Hz and a wobbler throw of 50 arcsec in azimuth. Pointing was checked frequently and was found to be stable to within 2.5 arcsec. Calibration was done every ∼10 min using the standard hot/cold-load absorber measurements. The data were recorded with the MPIfR Fast Fourier Transform spectrometers (FFTS; Klein et al. 2006) providing 4×2.5 GHz of bandwidth to cover the full 4 GHz bandwidth in each of the upper and lower sidebands of the sideband-separating FLASH receiver.

[1] Institute for Radio Astronomy in the Millimeter Range

[2] One source SPT0538-50 (Greve et al. 2012; Bothwell et al. 2013a), was not observed with ALMA.

Table 1. Observed [C II] and FIR properties. All luminosities are uncorrected for the lensing amplification. The upper limits for the velocity integrated fluxes given for the non-detections are obtained by assuming the FWHM observed for the CO lines. The total integration time with SPIRE FTS and FLASH is 92 h. The integration time per sources is given in the last column. †Full source names are listed in table 1 of Weiß et al. (2013) or in Table A1. [1]Has CO(1–0) observations (Aravena et al., in preparation). [2]Has CO(2–1) observations (Aravena et al., in preparation). ⋆See Bothwell et al. (2013b) for more details.

Source†	z	$SdV_{[C II]}$ (Jy km s^{-1})	dV (FWHM) (km s^{-1})	$L'_{[C II]}/10^{10}$ (K km s^{-1}/pc^2)	$L_{[C II]}$ (10^{10} L$_\odot$)	L_{FIR} (10^{13} L$_\odot$)	T_d (K)	$\frac{L_{[CII]}}{L_{FIR}}$ (10^{-4})	Instrument	Time (h)
SPT0551-50[1]	2.123	<180 (3σ)	–	<13.4	<3.0	1.1 ± 0.1	27.2 ± 1.0	<26.6	SPIRE FTS	3.8
SPT0512-59	2.234	227 ± 43	–	18.4 ± 3.5	4.0 ± 0.8	2.8 ± 0.2	33.2 ± 1.2	14.4 ± 2.9	SPIRE FTS	3.8
SPT0538-50[1]	2.782	<465 (3σ)	–	<81.9	<18.0	5.8 ± 0.3	36.9 ± 1.4	<31.0	SPIRE FTS⋆	3.8
SPT0103-45	3.090	125 ± 17	304 ± 47	17.5 ± 2.3	3.8 ± 0.5	3.4 ± 0.2	33.5 ± 1.1	11.3 ± 1.6	FLASH	2.7
SPT0550-53	3.129	129 ± 25	719 ± 124	18.5 ± 3.6	4.1 ± 0.8	1.6 ± 0.1	34.5 ± 1.8	25.4 ± 5.2	FLASH	17.3
SPT0529-54	3.369	217 ± 18	823 ± 92	35.1 ± 3.0	7.7 ± 0.7	3.0 ± 0.2	33.1 ± 1.2	25.7 ± 2.8	FLASH	3.8
SPT0532-50	3.399	113 ± 18	767 ± 124	18.6 ± 3.0	4.1 ± 0.7	6.5 ± 0.4	37.9 ± 1.4	6.3 ± 1.1	FLASH	4.6
SPT0300-46	3.596	41.5 ± 10.4	583 ± 138	7.5 ± 1.9	1.6 ± 0.4	3.3 ± 0.2	39.2 ± 1.5	5.0 ± 1.3	FLASH	12.8
SPT2147-50[2]	3.761	80.5 ± 11.7	329 ± 56	15.5 ± 2.3	3.4 ± 0.5	3.2 ± 0.2	41.4 ± 1.7	10.7 ± 1.7	FLASH	5.0
SPT0418-47[2]	4.224	127 ± 10	347 ± 29	29.5 ± 2.3	6.5 ± 0.5	5.9 ± 0.4	47.3 ± 2.5	11.0 ± 1.1	FLASH	1.5
SPT0113-46[2]	4.232	91 ± 19	619 ± 132	21.1 ± 4.4	4.6 ± 1.0	2.1 ± 0.1	32.9 ± 1.4	22.1 ± 4.8	FLASH	4.5
SPT2311-54	4.281	46.4 ± 5.3	360 ± 44	11.0 ± 1.2	2.4 ± 0.3	3.3 ± 0.3	43.3 ± 3.3	7.3 ± 1.1	FLASH	3.0
SPT0345-47[2]	4.296	63.7 ± 8.3	810 ± 200	15.2 ± 2.0	3.3 ± 0.4	9.2 ± 0.8	51.8 ± 3.2	3.6 ± 0.6	FLASH	2.3
SPT2103-60[2]	4.435	129 ± 18	780 ± 125	32.2 ± 4.4	7.1 ± 1.0	3.4 ± 0.2	39.2 ± 1.5	20.8 ± 3.1	FLASH	1.5
SPT0441-46[2]	4.477	42.5 ± 10.6	581 ± 162	10.8 ± 2.7	2.4 ± 0.6	3.7 ± 0.2	39.9 ± 1.9	6.6 ± 1.7	FLASH	3.2
SPT2146-55[2]	4.567	39.0 ± 9.0	302 ± 62	10.2 ± 2.4	2.2 ± 0.5	2.7 ± 0.3	39.2 ± 2.0	8.3 ± 2.1	FLASH	3.1
SPT2132-58	4.768	34.9 ± 6.9	212 ± 43	9.7 ± 1.9	2.1 ± 0.4	3.1 ± 0.3	39.5 ± 1.9	6.9 ± 1.5	FLASH	2.1
SPT2319-55	5.293	19.1 ± 3.2	198 ± 34	6.3 ± 1.1	1.4 ± 0.2	2.5 ± 0.2	42.0 ± 3.1	5.4 ± 1.1	FLASH	9.5
SPT0346-52[2]	5.656	63.3 ± 8.7	502 ± 72	22.8 ± 3.2	5.0 ± 0.7	12.3 ± 0.5	52.4 ± 2.2	4.1 ± 0.6	FLASH	1.4
SPT0243-49[2]	5.699	<51 (3σ)	–	<21.0	<4.5	3.3 ± 0.3	35.3 ± 1.6	<13.6	FLASH	2.2

The data were processed with the Continuum and Line Analysis Single-dish Software (CLASS[3]). We visually inspected the individual scans and omitted scans with unstable baselines, resulting in <10 per cent data loss. We subtracted linear baselines from the individual spectra in each of the two FFTS units, and regridded to a velocity resolution of ∼90 km s^{-1} in the averaged spectra. On-source integration times were between 1.5 and 5 h. Table 1 summarizes the line intensities, and Fig. 1 shows the spectra.

We detect [C II] emission in 16 out of 17 sources observed with FLASH. The only non-detection is in the highest redshift source, SPT0243-49 at $z = 5.699$. This source has an unambiguous redshift confirmed by two high-J CO lines with ALMA (Weiß et al. 2013) and a CO(2–1) line with ATCA (Aravena et al., in preparation). The observed $L_{[C II]}/L_{FIR}$ ratio ($<1.3 \times 10^{-3}$) is close to the median of our sample (see Table 1), suggesting that a [C II] detection for this source is feasible with a moderately deeper integration.

2.3 *Herschel*/SPIRE

For three $z \sim 2$ sources in the SPT sample (see Table 1), the [C II] line falls in a frequency range (500–610 GHz) where the atmosphere is opaque. We thus observed these sources with the SPIRE Fourier Transform Spectrometer (FTS; Griffin et al. 2010) onboard *Herschel*.[4] (Pilbratt et al. 2010). For more detail about the observations and results for SPT0538-50, see Bothwell et al. (2013b). The observations of SPT0551-50 and SPT0512-59 were carried out on 2013 March 2 in single-pointing mode using both the short wavelength (SSW) and long wavelength (SLW) bands covering 194–313 and 303–671 μm. The observations were done in high spectral resolution mode equivalent to 0.04 cm^{-1} (1.2 GHz) with 100 repetitions, resulting in an on-source integration time of 13752 s (3.8 h) per source.

The data were reduced and calibrated using an updated SPIRE FTS pipeline in the *Herschel* reduction tool HIPE v11, which includes all detectors in the observation and uses new calibration files. The detection of lines fainter than 1 Jy is very challenging because thermal emission from the warm optics contributes as much as 1000 Jy at 1000 GHz. We subtract the average of the off-target pixels in order to remove this excess emission from the telescope. Another possibility is to subtract a 'dark sky' observation made on the same day with the same exposure time, but in our case the noise level was lowest by subtracting the average of the off-target pixels. As the model of the telescope has an uncertainty of 0.1 per cent, there remains a residual continuum uncertainty of ∼1 Jy in the continuum. We therefore subtract an additional second-order polynomial from the SSW and the SLW spectral part separately, and look for the [C II] line at the expected frequency (Valtchanov et al. 2011). Fig. 2 shows the resulting spectra.

3 RESULTS

Figs 1 and 2 show the [C II] emission lines and Table 1 lists the [C II] luminosities obtained from APEX/FLASH and *Herschel* SPIRE FTS observations, along with far-IR (FIR) luminosities (L_{FIR}). We have 17 [C II] emission line detections (16 with FLASH and one with *Herschel* SPIRE FTS) and three non-detections (one with FLASH and two with *Herschel* SPIRE FTS).

3.1 Velocity profiles and line fluxes

Despite an increasing number of high-z [C II] detections in the literature, only a few of these have sufficient spectral resolution and

[3] http://www.iram.fr/IRAMFR/GILDAS/

[4] *Herschel* is an ESA space observatory with science instruments provided by European-led Principal Investigator consortia and with important participation from NASA.

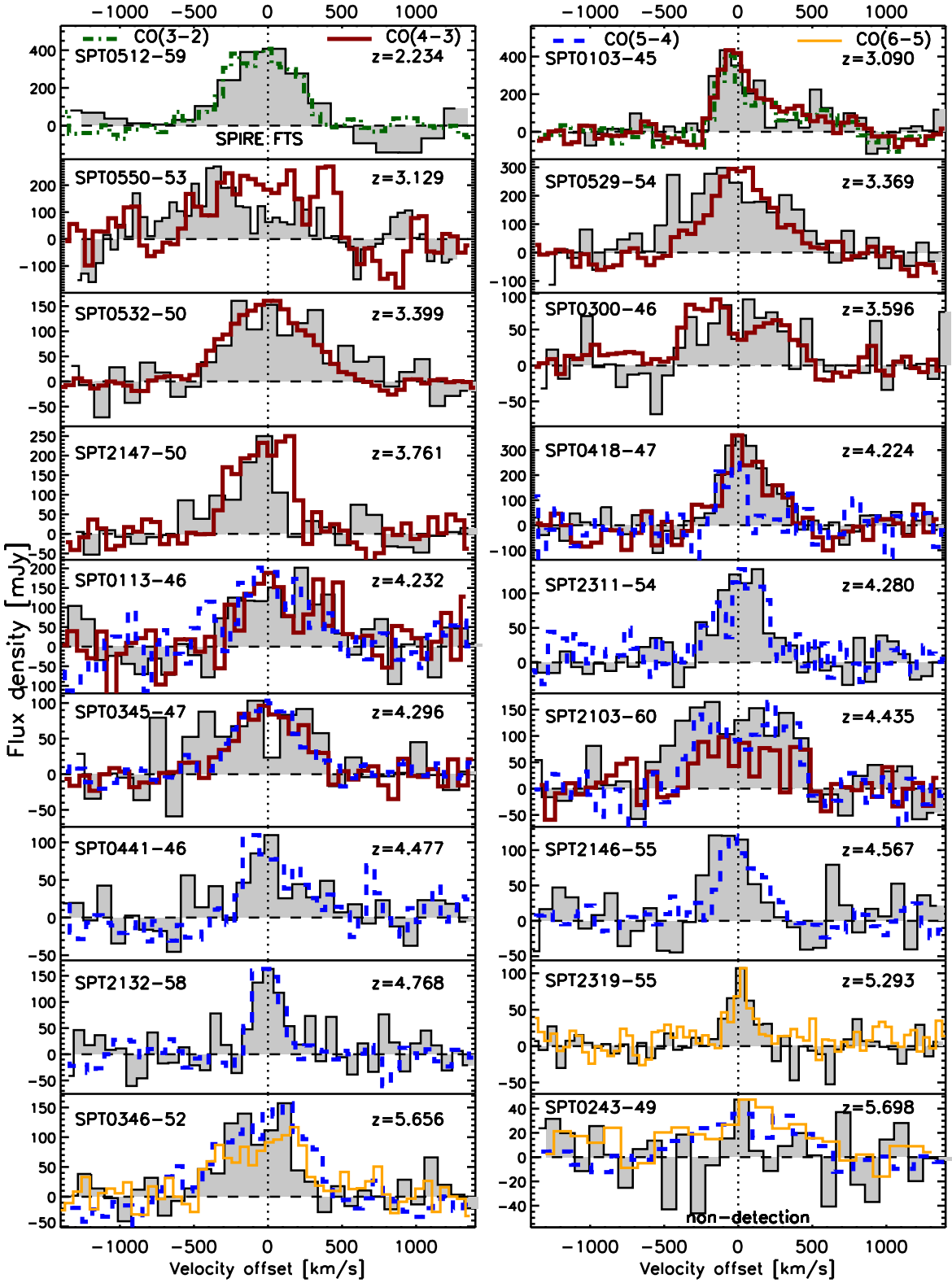

Figure 1. Comparison of the velocity profiles of the [C II] lines detected with APEX/FLASH and SPIRE FTS (grey filled profiles) and mid-*J* CO line observed with ALMA in Cycle 0 (coloured lines; Weiß et al. 2013). The CO lines have been scaled to match the [C II]peak flux. The similarities between the CO and [C II] lines for individual sources suggest that the spatial distributions are similar and differential lensing is not significant.

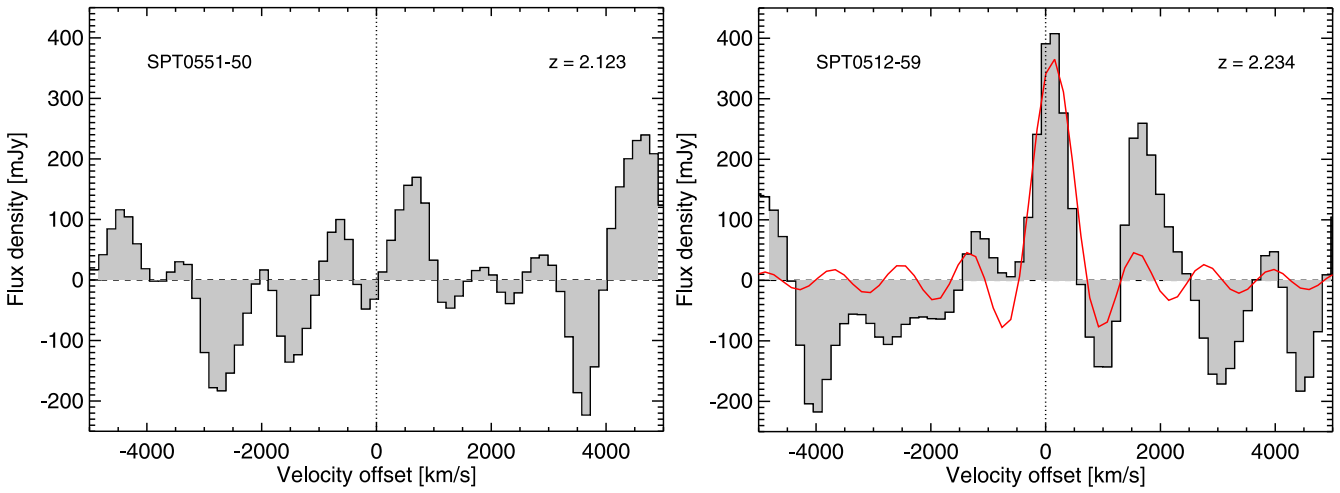

Figure 2. *Herschel* SPIRE FTS spectra for SPT0551-50 and SPT0512-59. Left: non-detection of the [C II] emission line for SPT0551-50. Right: detection of [C II] emission line for SPT0512-59. The continuous red curve is the sinc function used to fit the [C II] line (see Valtchanov et al. 2011).

S/N and supporting data to compare line profiles with other bright lines like CO (e.g. Rawle et al. 2014). This is the first sample of sources with spectrally resolved data with S/N≥3 in *both* [C II] and CO making it possible to compare the shapes of velocity profiles. In the following, we consider only the 17 sources observed with FLASH, as the three sources observed with SPIRE are not spectrally resolved.

Fig. 1 shows the velocity profiles of the [C II] lines compared with the mid- and high-*J* CO lines observed with ALMA. The CO lines have been scaled to match the peak flux of the [C II] line, in order to facilitate the comparison of the velocity profiles. We first fit the CO and the [C II] lines independently with single Gaussian functions. We accept the single Gaussian fit if the reduced χ^2 does not exceed $1+5\times\sqrt{2n_{\rm dof}}$, where $n_{\rm dof}$ is the number of degrees of freedom. This quantity corresponds to five standard deviations of the χ^2 distribution. If the single Gaussian fit does not match the above criterion, we use a double Gaussian function, i.e. two Gaussian functions with displaced central positions. The double Gaussian function is sufficient to describe the line profiles that do not match a single Gaussian. In practice, this happens in SPT0103-45 and SPT0418-47, which have lines that display a slight asymmetry on the red side of the lines; the velocity difference between the CO and [C II] peaks is <150 km s^{-1}.

We then simultaneously fit the single or double Gaussian profile (depending on what is necessary to fit the profiles individually) to the CO and [C II] velocity profiles assuming the profiles are similar with just one free scaling parameter. This allows us to test if the two profiles are consistent or not. Only the [C II] and CO lines for SPT0532-50 have different velocity profiles. The remaining 16 sources have consistent line profiles with $\chi^2 < 1 + 5 \times \sqrt{2n_{\rm dof}}$.

We obtain the line widths (FWHM) listed in Table 1 by fitting a single Gaussian. To test the reliability of our method we also fit the spectra by taking velocity-weighted moments, and find fully consistent results. The resulting full width at half-maximum (FWHMs) are in the range ∼210–820 km s^{-1}. This is comparable to the typical CO line width of ∼460 km s^{-1} found for SPT DSFGs by stacking 22 spectra (Spilker et al. 2014). Nine out of 20 sources have FWHM >500 km s^{-1}, which is large compared to other high-z [C II] detections (e.g. 360 km s^{-1} on average in the sample of Wang et al. 2013).

We obtain the velocity-integrated fluxes for the FLASH/APEX detections by summing the observed line profiles over the 3σ limits obtained from the single Gaussian fits. The [C II] apparent luminosities range from 1.4 to 9.2 $\times$ 10^{10} L$_\odot$ which is 1–2 orders of magnitude higher than their mid- and high-*J* CO luminosities (∼3 − 30 $\times$ 10^8 L$_\odot$), where both are uncorrected for lensing.

The [C II] detection in SPT0512-59 with SPIRE FTS (see Fig. 2 *right*) confirms the redshift at $z = 2.234$. We determine the integrated line flux in the same manner as Valtchanov et al. (2011) by fitting the emission lines with a sinc function, and calculate the rms using the standard deviation of each channel within ±5000 km s^{-1} of the expected line centroid (see Valtchanov et al. 2011 for more details).

Our SPIRE FTS observation for SPT0551-50[5] does not detect any [C II] emission (see Fig. 2 *left*). The redshift was reconfirmed by weak CO(1–0) emission observed with ATCA (Aravena et al., in preparation). We therefore take the 3σ upper limit of the expected line peak to be three times the rms noise.

3.2 Lensing

The lensing magnification of the SPT DSFGs allows us to study the ISM in galaxies at high redshifts, but also introduces the possibility of differential lensing. The compactness and location of a region relative to the lensing caustic determines the magnification of the emission. Differential lensing amplification may thus occur between compact and extended emitting regions, or components occupying different regions (e.g. Hezaveh, Marrone & Holder 2012). From observations of the Milky Way and nearby galaxies, we might expect the [C II] emission to originate from more extended and diffuse media than the more optically thick low-*J* CO emission in giant molecular clouds (GMCs) (Fixsen, Bennett & Mather 1999). If the [C II] was dominated by emission from such diffuse regions, it could be subject to differential lensing compared to the more compact CO emission. However, the similar [C II] and CO velocity profiles suggest that such differential lensing is not significant.

[5] Note that is one of the rare cluster lenses in the SPT sample (Vieira et al. 2013). This, however, should not have any effect on the detectability of [C II] in this source.

Modelling the lensing magnification factor is of great importance, and has been performed for some of the DSFGs in this sample using ALMA data. The lens modelling is performed in the (u, v)-plane to properly represent the parameter uncertainties in the interferometric data (see Hezaveh et al. 2013 for more details). The four sources with lens models have lensing magnification factors μ between ∼5.4 and 21.0 (Hezaveh et al. 2013) and a mean of $\langle\mu\rangle = 14.1$. In cases where the lensing magnification factor is unknown, we use the mean magnification factor to estimate the intrinsic luminosity. We then conservatively choose to span the uncertainty on the lensing magnification factor from the smallest ($\mu = 5.4$) to the largest ($\mu = 21.0$) giving the mean magnification an uncertainty of 7.8. We assume that the magnification factors derived from the dust continuum are also appropriate for the line-emitting gas. A lens modelling analysis of the remainder of the ALMA Cycle 0 imaging data is currently under way.

4 ANALYSIS

4.1 Comparison sample of nearby and distant galaxies

We compare the SPT sample with that of Gracia-Carpio et al. (in preparation), which is comprised of 333 sources. These sources include LIRGs and ULIRGs from the Great Observatories All-sky Survey (GOALS; Díaz-Santos et al. 2013) and normal and Seyfert galaxies from Brauher et al. (2008) with spatially unresolved [C II] detections integrated over the entire individual galaxies. The sample contains 308 sources at $z < 0.4$ and 25 at $z > 1$. In addition, we have searched the literature for additional $z > 1$ DSFGs with [C II] observations, which we list in Appendix B. In constructing this low- and high-z comparison sample, we have paid particular attention to ensure that the photometric data are integrated over the full galaxies, as all line and continuum data for the SPT sample are also integrated values.

4.1.1 Conversion to CO(1–0) luminosities

Like the SPT sample (Section 2.1), many of the sources in the comparison sample also have published CO observations. In cases where the CO(1–0) emission lines have not been observed, Gracia-Carpio et al. (in preparation) derive the $L_{\rm CO(1-0)}$ by converting the observed mid-J CO luminosities to $L_{\rm CO(1-0)}$ using scaling factors from Stacey et al. (2010). When multiple $J > 1$ CO lines were observed, we take the average of the scaled $L_{\rm CO(1-0)}$. These scaling factors are based on previous studies involving several rotational lines from both nearby galaxies, ULIRGs and high-z galaxies (Stacey et al. 2010), which allow for the assumption of fixed CO line ratios up to CO(4–3)/CO(1–0). The conversion factors used by Stacey et al. (2010) assume an integrated line flux (W m^{-2}) ratio of CO(2–1)/CO(1–0) = 7.2, equivalent to 90 per cent of the thermalized optically thick emission (i.e. a brightness temperature ratio of 0.9), CO(3–2)/CO(2–1) = 3.0 (90 per cent of the thermalized optically thick emission) and CO(4–3)/CO(2–1) = 6.4 (80 per cent of the thermalized optically thick emission).

The assumed CO(2–1) to CO(1–0) brightness temperature ratio of 0.9 for DSFGs is in agreement with observations of Bothwell et al. (2013a), who find a ratio of 0.85 for 32 luminous submm galaxies at $z \sim 1.2$–4.1. The [CO(2–1)/CO(1–0)] ratio has also been observed for four normal star-forming galaxies by Aravena et al. (2014), resulting in a slightly lower [CO(2–1)/CO(1–0)] brightness temperature ratio of 0.7 ± 0.16 for four BzK galaxies at $z \sim 1.5$–2.2. Even though the ratio is consistent with Bothwell et al. (2013a) within the uncertainties, a lower [CO(2–1)/CO(1–0)] ratio is expected for normal star-forming galaxies than for starburst galaxies, because the molecular gas in starburst galaxies is expected to be more highly excited. Spilker et al. (2014) find an average CO(2–1)/CO(1–0) brightness temperature ratio of 1.1 ± 0.1 for 22 of the SPT DSFGs by stacking ATCA spectra, after scaling them by their 1.4 mm continuum flux density. Given the range of values of these three methods, and for consistency with previous literature, we adopt the scaling factor of 0.9 from Stacey et al. (2010).

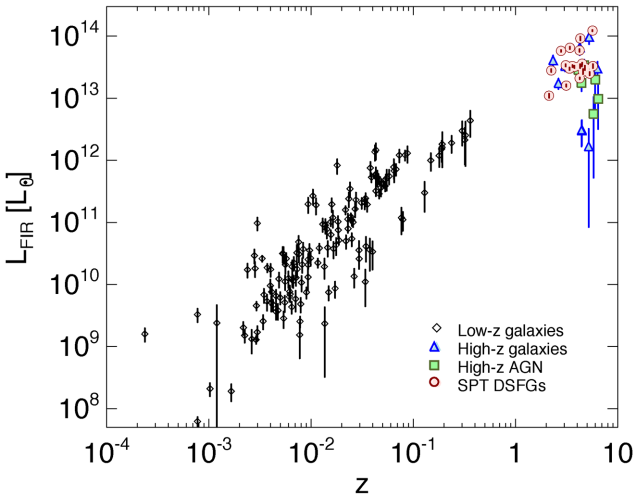

Figure 3. Observed $L_{\rm FIR}$ versus redshift for the 20 SPT sources and the comparison sample. No $L_{\rm FIR}$ have been corrected for lensing magnification factors. The distribution shows the Malmquist bias where high-z galaxies require either lensing magnification or very high intrinsic FIR luminosity of $L_{\rm FIR} \gtrsim 10^{12}$ L$_\odot$ to be included in the parent sample. The evolution of the luminosity function and the smaller comoving volume at low redshifts imply that objects with similar high intrinsic $L_{\rm FIR}$ are missing from the low-z sample. However, the most highly lensed DSFGs may have similar intrinsic $L_{\rm FIR}$ than the most luminous sources in the local sample.

4.1.2 FIR luminosities

We obtain the FIR luminosities $L_{\rm FIR}$ and the dust temperature $T_{\rm d}$ for each source in the SPT DSFG sample by fitting the well-sampled spectral energy distributions (SEDs) with a greybody law fixing the emissivity index (β) at 2.0, $\mu_0 = 100$ and fitting $\lambda_{\rm rest} < 50$ μm, following Greve et al. (2012) and Strandet et al. (in preparation). We integrate the SED between $\lambda_{\rm rest} = 42$-500 μm in the rest frame to obtain $L_{\rm FIR}$. Our SPT DSFGs all have seven photometric data points covering observed wavelengths from 250 to 3000 μm (e.g. Weiß et al. 2013). This allows for a uniform determination of the FIR luminosity using a parametrized SED fitting.[6] The SPT sources, which have well-sampled SEDs, thus have a smaller uncertainty in $L_{\rm FIR}$ than sources with poor photometric coverage (see Fig. 3).

To compare the low-z and high-z sample with the SPT sources in a consistent way, we compiled published FIR photometry (Gracia-Carpio et al., in preparation; Appendix B), and derived $L_{\rm FIR}$ and $T_{\rm d}$ using the same fitting code we used for the SPT sources (Greve et al. 2012). *IRAS* and *ISO* data are available for sources published by Brauher et al. (2008), and FIR data are also available for a

[6] Other studies (e.g. Stacey et al. 2010; Helou et al. 1988) use the two-band definition for $L_{\rm FIR}$: $F_{\rm FIR} = 1.26 \times 10^{-14} \times (2.58 f_{60} + f_{100})$[W m^{-2}] which is equivalent to the 42.5–122.5 μm luminosity (Helou et al. 1988).

large number of the GOALS sources at NASA/IPAC Extragalactic Database (NED[7]). The comparison sample contains 165 sources with sufficiently good photometry to derive $L_{\rm FIR}$ and $T_{\rm d}$ using the method in Greve et al. (2012); 14 of these are $z > 1$ sources (see Fig. 3). Sources with insufficient available photometry to derive $L_{\rm FIR}$ using our procedure are not included in analyses requiring $L_{\rm FIR}$ but are still included in the $L_{\rm [C\,II]}/L_{\rm CO(1-0)}$ ratios.

Fig. 3 presents the observed $L_{\rm FIR}$ distribution of our combined sample. There is a clear gap between the low- and high-z samples due to the limited sensitivity of the nearby samples, and the atmospheric transparency prohibiting [C II] observations at $z < 1$ from the ground. The selection function of the high-z sample is quite complex because many sources have been pre-selected to have a good chance of detection in [C II] (e.g. by having strong dust continuum and/or CO emission). In addition, the improved atmospheric transparency at lower frequencies mostly compensates for the distance dimming in the more distant sources. The evolution of the luminosity function and the smaller comoving volume at low redshifts imply that objects with similar high intrinsic $L_{\rm FIR}$ are missing from the low-z sample.

The SPT sources in this sample have FIR luminosities in the range $L_{\rm FIR}$=(1.2–11.8) $\times$ 10^{13}L$_\odot$. After de-magnification, the range is $L_{\rm FIR}/\mu$ = (1.1–21.9) $\times$ 10^{12} L$_\odot$, with a mean de-magnified $L_{\rm FIR}$ of 5.2 $\times$ 10^{12} L$_\odot$, which is similar to the most luminous sources in the low-z sample.

The uniform sensitivity of the ALMA mm spectroscopy, continuum, low-J CO, and [C II] observations (all with S/N > 3) lead to a high completeness of the SPT sample. This, combined with the lensing amplification factor which is about one order of magnitude (Hezaveh et al. 2013), make the SPT DSFG sample one of the most representative samples to date for massive, IR-luminous starburst galaxies at high redshifts.

4.1.3 AGN content

The comparison sample contains both starburst galaxies and luminous AGN. In the high-redshift sample, we distinguish the AGN-dominated sources from those without any known AGN. These high-redshift AGN are quite rare sources, mostly selected based on their bright optical emission lines (e.g. Wang et al. 2013). The SPT DSFGs are selected solely on their lensed 1.4 mm continuum flux, and direct mm imaging and spectroscopy avoids any radio/optical identification steps that may introduce biases towards AGN-dominated systems. Optical spectroscopy of the SPT DSFG sample to derive the redshifts of the foreground lensing galaxies has not shown any indications of type-1 or type-2 AGN. Strongly obscured type-2 AGN may still be present in some SPT DSFGs. Supported by the discussion in Section 4.4, we will assume in the following that the AGN contributions in the SPT DSFGs are negligible.

4.2 Observed [C II] to FIR ratios

Fig. 4 presents the $L_{\rm [C\,II]}/L_{\rm FIR}$ ratio against $L_{\rm FIR}$ for the SPT sources and the comparison sample. The typical error bar for the low-z sources (in this and the following plots) is illustrated by the cross in the bottom left. This typical error bar includes the quoted uncertainties of the lines (e.g. Young et al. 1995; Negishi et al. 2001), the absolute and statistical uncertainty of the FIR photometry, and

[7] http://ned.ipac.caltech.edu

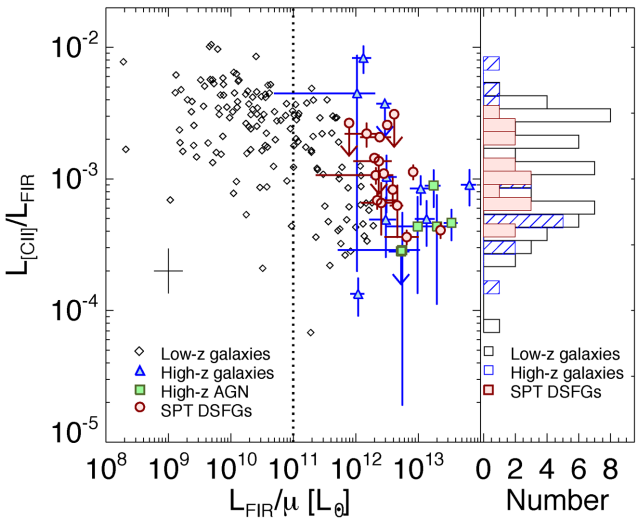

Figure 4. $L_{\rm [C\,II]}/L_{\rm FIR}$ versus $L_{\rm FIR}$ for SPT sources and the comparison sample. As reported in previous versions of this plot, the $L_{\rm [C\,II]}/L_{\rm FIR}$ is anticorrelated with $L_{\rm FIR}$. In particular at $L \gtrsim 10^{11}$ L$_\odot$, the $L_{\rm [C\,II]}/L_{\rm FIR}$ ratio drops and has a larger spread. For the SPT sources without known lensing models, we assume a lensing magnification factor of 14.1 (and an uncertainty which encompasses the range of 5 to 22 from the known models). The typical error bar for the literature sources is represented by the black cross in the lower left. The histogram on the right shows the distribution of galaxies with $L_{\rm FIR} \gtrsim 10^{11}$ L$_\odot$.

of the FIR luminosity determined by our own SED fitting. The SPT DSFGs have been corrected for lensing amplification either using the known lens model (Hezaveh et al. 2013), or assuming a mean magnification factor $\langle\mu\rangle = 14.1 \pm 7.8$ for the sources without a lens model (see Section 3.2).

Sources with $L_{\rm FIR} \lesssim 10^{11}$ L$_\odot$ appear to have a roughly constant $L_{\rm [C\,II]}/L_{\rm FIR}$ ratio ($\sim 4 \times 10^{-3}$). At $L_{\rm FIR} \gtrsim 10^{11}$ L$_\odot$, the ratio drops to 6×10^{-4} for the $z < 1$ sources in the comparison sample, similar to what has been reported in previous studies (e.g. Maiolino et al. 2009; Stacey et al. 2010). Whether this is an intrinsic or observational effect due to limited sensitivity of the [C II] and/or FIR photometry in the low-z samples is not clear, and investigating this is beyond the scope of this paper. The $z > 1$ sources from the comparison sample are scattered over two orders of magnitude, which may be due to the heterogeneous mix of the parent samples. The highly complete (82 per cent detections) and uniformly observed SPT sources have a smaller scatter and an average $L_{\rm [C\,II]}/L_{\rm FIR}$ ratio of $\sim 10^{-3}$. A Kolmogorov–Smirnov test results in a probability of 0.7 that the $L_{\rm [C\,II]}/L_{\rm FIR}$ values for $L_{\rm FIR} \gtrsim 10^{11}$ L$_\odot$ from the SPT and the low-z samples are drawn from the same distribution.

Normalizing the FIR luminosity by the molecular gas mass reduces the scatter seen in Fig. 4 for the $L_{\rm FIR} \gtrsim 10^{11}$ L$_\odot$ sources (Graciá-Carpio et al. 2011). The $L_{\rm FIR}/M_{\rm H_2}$ ratio is expected to be proportional to the star formation efficiency, specifically to the number of stars formed in a galaxy per unit molecular gas mass. This ratio has the additional advantage that the lensing magnification factor cancels out. We estimate the molecular gas masses for the 11 sources for which we also have low-J CO line detections (Aravena et al., in preparation). We determine the molecular gas mass by

$$M_{\rm H_2} = \alpha_{\rm CO} L'_{\rm CO(1-0)}, \quad (1)$$

where $\alpha_{\rm CO}$ is the CO-to-H$_2$ conversion factor. To be consistent with Graciá-Carpio et al. (2011), we assume $\alpha_{\rm CO}$ = 0.8 M$_\odot$ (K km s^{-1} pc^2)$^{-1}$ determined by Downes & Solomon

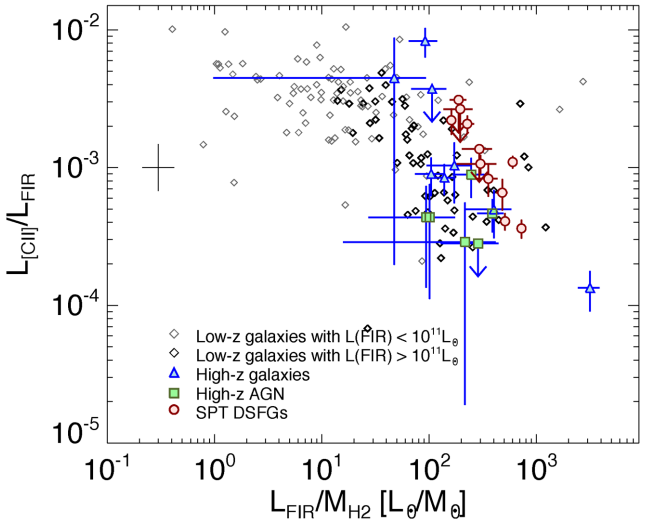

Figure 5. $L_{[C\,II]}/L_{FIR}$ versus the FIR luminosity normalized by the molecular gas mass. The molecular gas mass is derived assuming a conversion factor of $\alpha_{CO} = 0.8\,M_\odot$ (K km s^{-1} pc^{-2})$^{-1}$. The L_{FIR}/M_{H_2} ratio is expected to be proportional to the number of stars formed in a galaxy per unit molecular gas mass (Graciá-Carpio et al. 2011). This M_{H_2} normalization removes the uncertainty due to the unknown lensing magnification factors, and reduces the scatter seen in Fig. 4, but the deficit in the $L_{[C\,II]}/L_{FIR}$ ratio still persists. The typical error bar is represented by the black cross.

(1998) for the SPT DSFGs and the low- and high-z comparison samples. Fig. 5 plots $L_{[C\,II]}/L_{FIR}$ as a function of L_{FIR}/M_{H_2} and shows that the DSFGs lie among the local LIRGs. Low-z sources with $L_{FIR} \gtrsim 10^{11}\,L_\odot$ and the high-z sources have similar $L_{[C\,II]}/L_{FIR}$ ratios.

4.3 Dust temperatures

As first shown by Malhotra et al. (1997), the $L_{[C\,II]}/L_{FIR}$ ratio shows a strong anticorrelation with T_d. They attributed this trend to an increase in the G_0/n ratio (far-UV ionizing field over density) in the hotter, more active galaxies, and hence a lower efficiency of gas heating reducing the [C II] flux while increasing the dust temperature. We here revisit this trend using the uniformly derived set of L_{FIR} and T_d values for the SPT sources and comparison samples, derived from our SED modelling (Section 4.1). The top panel of Fig. 6 compares the $L_{[C\,II]}/L_{FIR}$ ratio to T_d, with both quantities being independent of the lensing magnification. The strong anticorrelation of these quantities is visible in all three samples. However, if the dust and [C II] emission are coming from the same regions, and $L_{[C\,II]}$ is less dependent on T_d, a significant part of this anticorrelation can be explained with the Stefan–Boltzmann law which predicts $L_{FIR} \propto {T_d}^4$.

In order to look for a residual correlation, we cancel out the $L_{FIR} \propto {T_d}^4$ dependence by plotting $L_{[C\,II]} \times {T_d}^4/L_{FIR}$ against T_d (see bottom panel of Fig. 6). We note that a small systematic offset in T_d would get propagated as ${T_d}^4$. To test the presence of a correlation taking into account the [C II] upper limits, we use the generalized Kendall's tau method (Lavalley, Isobe & Feigelson 1992). We find a probability that both variables are not correlated of 0.036, 0.602, and 0.151 for the low-z, high-z and SPT samples, respectively. The small displacement of the SPT sources relative to the comparison sample in Fig. 6 is likely due to Malmquist bias and evolution effects resulting in the most luminous sources being absent in the low-z comparison sample (see Section 4.1.2). While there is marginal

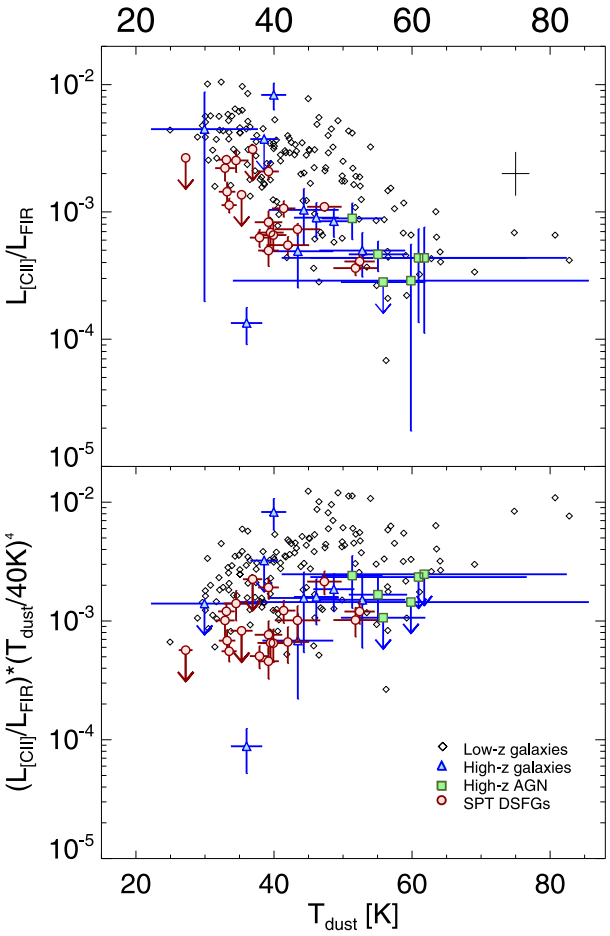

Figure 6. Top panel: $L_{[C\,II]}/L_{FIR}$ versus T_d for the SPT DSFGs and the low- and high-z comparison sample. The anticorrelation between the $L_{[C\,II]}/L_{FIR}$ ratios and the dust temperatures is seen for both low- and high-z sources, and is expected because the Stefan–Boltzmann law predicts $L_{FIR} \propto 1{T_d}^4$. Bottom panel: [C II]$\times {T_d}^4/L_{FIR}$ versus T_d for the SPT DSFGs and the low- and high-z comparison sample. Multiplying the $L_{[C\,II]}/L_{FIR}$ ratio with ${T_d}^4$ cancels out the temperature dependence of the Stefan–Boltzmann law. All lensing magnification factors and beam filling factors cancel in both panels, and the typical error bar is represented by the black cross.

evidence for a small positive residual correlation (especially in the low-z sample), most of the correlation seen in the top panel has cancelled out. This confirms our assumptions that the dust and [C II] emission are originating from the same regions and that $L_{[C\,II]}$ is less dependent on T_d. We therefore conclude that the observed correlation is mostly dominated by the Stefan–Boltzmann law.

4.4 Observed [C II] to CO ratios

One of the strengths of the SPT DSFG sample is that more than half of the sources have both [C II] and low-J CO detections. Fig. 7 plots the [C II] versus CO(1–0) luminosities for these 11 sources, along with high-z sources in the comparison sample.[8] All high-z

[8] Note that Fig. 7 presents a larger number of high-z sources than Figs 5, 6, and 8, as it does not involve quantities derived from continuum photometry. The calculation of L_{FIR} and T_d require photometric data that are unavailable for several of the high-z comparison objects (see Section 4.1 and Appendix B).

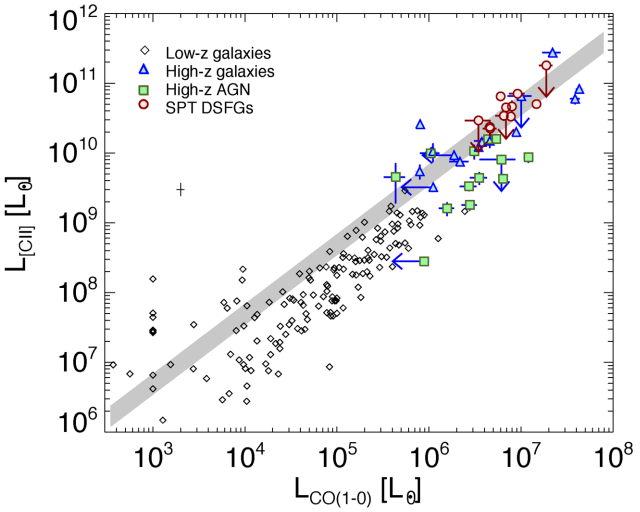

Figure 7. The [C II] luminosity versus the CO luminosity for the SPT DSFGs and the comparison low- and high-z samples. These star-forming systems show a correlation between the [C II] and CO(1–0) luminosities. Fitting a ratio to 11 SPT sources with [C II] detections and CO(1–0) data yields a slope of ∼5200. The width of the grey shaded area represents a 1σ spread, ∼5200 ± 1800. Fitting a ratio to the low-z sample yields a slope of 1300 ± 440. The typical error bar for the low-z sources is represented by the black cross.

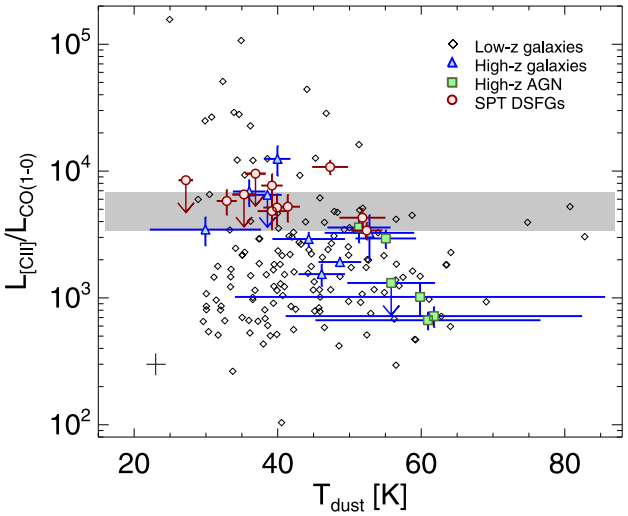

Figure 8. $L_{[C\,II]}/L_{CO(1-0)}$ versus T_d for the SPT sources and the low- and high-z comparison sample. The typical error bar is represented by the black cross. The grey shaded area represents the 1σ spread of the $L_{[C\,II]}/L_{CO(1-0)}$ ratio in the SPT sample. Both the SPT sources and the low-z sample do not show any dependence on T_d. The high-z AGN-dominated sources are both warmer and have fainter [C II] relative to CO.

sources fall close to the $L_{[C\,II]}/L_{CO(1-0)}$ ∼4400 relation for local galaxies reported by Crawford et al. (1985), Wolfire, Hollenbach & Tielens (1989), Stacey et al. (1991a, 2010), Swinbank et al. (2012), Neri et al. (2014). This relation has been explained in terms of PDR models (Wolfire, Hollenbach & Tielens 1989, 1993; Stacey et al. 1991a). Using the eight SPT DSFGs with [C II] and CO(1–0) detections, we determine the $L_{[C\,II]}/L_{CO(1-0)}$ ratio to be 5200 ± 1800. In Section 5.1, we derive the physical conditions that can be derived from this ratio from first principles and eventually compare it with the PDR models.

Finally, in Fig. 8, we test if the $L_{[C\,II]}/L_{CO(1-0)}$ ratio[9] depends on T_d. We find no correlation in either the low-z or the SPT DFSG sample. However, the four high-z sources with the lowest $L_{[C\,II]}/L_{CO(1-0)}$ ratio are all AGN dominated. This is consistent with the observations of Stacey et al. (2010) and Sargsyan et al. (2014) that AGN-dominated sources have lower $L_{[C\,II]}/L_{FIR}$ ratios. Although our T_d determinations are rather crude, these AGN-dominated sources are also those with the warmest T_d, as expected (see e.g. fig. 3 in Greve et al. 2012). Interestingly, only 2 out of 11 SPT DSFGs fall near the AGN-dominated sources in Fig. 8, supporting our conclusion (Section 4.1.3) that the SPT sample does not contain many strongly AGN-dominated sources.

5 DISCUSSION

5.1 Possible origins of the [C II] to CO correlation

5.1.1 Determining the optical depth of the [C II] line

The origin of the correlation between the [C II] and CO(1–0) luminosities and the impact of their relative optical depths was first discussed by Crawford et al. (1985), and later by others in both low- and high-z objects (e.g. Wolfire et al. 1989; Stacey et al. 1991a, 2010; Swinbank et al. 2012; Neri et al. 2014). Crawford et al. (1985) assumed [C II] excitation temperatures $T_{ex,[C\,II]} \gg 92$ K,[10] and could therefore apply the Rayleigh–Jeans approximation. This assumption was supported by independent estimates of the gas temperature of order ∼300 K using other fine structure lines and assuming optically thin [C II] emission (Ellis & Werner 1984). They remarked that their observed $L_{[C\,II]}/L_{CO(1-0)}$ ratio ∼4400 is close to the [C II] to CO(1–0) frequency ratio cubed, suggesting optically thick [C II] emission. However, using supporting data in Orion, the Galactic Centre and M82, they independently derived [C II] optical depths $\tau_{[C\,II]} = 0.03-1$. This conclusion that [C II] is mostly optically thin has been assumed several times since (e.g. Stacey et al. 1991a; Hailey-Dunsheath et al. 2010; Stacey et al. 2010; De Breuck et al. 2011; Rawle et al. 2014).

The most accurate way to determine the optical depth of the [^{12}C II] emission line is through observations of the isotopic line ratios. The two [C II] emission lines for ^{12}C and ^{13}C have been observed in local star-forming regions, e.g. in M42 (Stacey et al. 1991b; Boreiko & Betz 1996), NGC2024 (in the Orion nebula; Graf et al. 2012), the Orion Bar, Mon R2, NGC 3603, the Carina Nebula and NGC 7023 (Ossenkopf et al. 2013). These observations find optical depths ranging from $\tau \sim 1$ to $\tau \sim 3$, with on average a moderate optical dept $\tau \sim 1.4$. However, one should keep in mind that Orion and Carina are very bright [C II] emitters (to allow for a detection of the faint ^{13}C), with very strong far-ultraviolet (FUV) fields ($G_0 \sim 10^4$–10^5), implying large [C II] columns and hence rather high opacities. The galaxy-scale average may result in lower optical depths near unity. Unfortunately, this isotope ratio technique cannot be applied to galaxy-integrated [C II] observations as the [^{12}C II] fine structure line and the brightest [^{13}C II] hyperfine structure line are only separated by ∼110 km s^{-1}, which is smaller than the typical widths of these lines. The much weaker ^{13}C line is then indistinguishable from features in the profile of the ^{12}C line.

[9] Note that both parameters are independent of the lensing magnification.

[10] The [C II] ground state energy level is 92 K.

The optical depth of [C II] in very distant galaxies must therefore be estimated by other methods. The idea of optically thick [C II] emission at high redshifts was recently proposed by Neri et al. (2014) for the high-z sub-millimetre source HDF 850.1. Assuming the [C II] line excitation temperature is the same as the dust and gas kinetic temperatures, they argue for high line optical depth of the [C II] line (i.e. $\tau_{[\mathrm{C\,II}]} \gtrsim 1$). The observed $L_{[\mathrm{C\,II}]}$ and predicted $L_{\mathrm{CO}(1-0)}$ by Walter et al. (2012), yield a $L_{[\mathrm{C\,II}]}/L_{\mathrm{CO}(1-0)}$ ratio of ∼5200, in agreement with the ratio derived from the SPT sample of 5200 ± 1800 (Section 4.4). We now generalize this line ratio method by comparing the source functions. This does not require the CO and [C II] excitation temperatures to be the same, nor that the Rayleigh–Jeans approximation applies (i.e. we also consider cases where $T_{\mathrm{ex},[\mathrm{C\,II}]}$ is close to or below 91 K).

From the source functions of both lines, the luminosity ratio depends on

$$\frac{L_{[\mathrm{CII}]}}{L_{\mathrm{CO}(1-0)}} = \left(\frac{\nu_{[\mathrm{CII}]}}{\nu_{\mathrm{CO}(1-0)}}\right)^3 \times \left(\frac{\Delta\nu_{[\mathrm{CII}]}}{\Delta\nu_{\mathrm{CO}(1-0)}}\right) \times \frac{\mathrm{e}^{h\nu_{\mathrm{CO}(1-0)}/kT_{\mathrm{ex,CO}(1-0)}} - 1}{\mathrm{e}^{h\nu_{[\mathrm{CII}]}/kT_{\mathrm{ex},[\mathrm{CII}]}} - 1} \times \frac{1-\mathrm{e}^{-\tau_{[\mathrm{CII}]}}}{1-\mathrm{e}^{-\tau_{\mathrm{CO}(1-0)}}}, \quad (2)$$

where we have assumed that the [C II] and CO emitting gas have the same filling factors (see Section 4.3). This assumption is consistent with the very similar [C II] and CO velocity profiles (Fig. 1). In this case, $\frac{\Delta\nu_{[\mathrm{CII}]}}{\Delta\nu_{\mathrm{CO}(1-0)}} = \frac{\nu_{[\mathrm{CII}]}}{\nu_{\mathrm{CO}(1-0)}}$. Also in nearby galaxies, [C II] and CO have been found to trace each other both morphologically and kinematically (e.g. Mittal et al. 2011; Braine et al. 2012). Equation (2) has four free parameters: two excitation temperatures and two opacities. In order to obtain constraints, we therefore have to fix some of these.

5.1.2 *Same [C II] and CO excitation temperatures*

We first consider the case suggested by Neri et al. (2014) of equal excitation temperatures (i.e. $T_{\mathrm{ex},[\mathrm{C\,II}]} = T_{\mathrm{ex,CO}(1-0)}$), Fig. 9 plots $L_{[\mathrm{C\,II}]}/L_{\mathrm{CO}(1-0)}$ versus T_{ex} for the three scenarios: (i) optically thin [C II] and (nearly) optically thick CO(1–0) emission, (ii) (nearly) optically thick [C II] and optically thin CO(1–0) emission, (iii) same optical depth for [C II] and CO(1–0).

Scenario (i) shown by the black dot–dashed curve underpredicts the observed ratio (grey shaded area) by an order of magnitude. In the opposite case, scenario (ii) (grey dot–dashed curve), the observed ratio is reached only for very low excitation temperatures. However, this optically thin CO scenario can be ruled out because both the ^{12}CO to ^{13}CO ratios and the low-J ^{12}CO line ratios in the SPT sample imply that CO is moderately optically thick with $\tau_{\mathrm{CO}(1-0)}$=1–10 (Spilker et al. 2014), similar to what is seen in our own galaxy (Penzias et al. 1972; Goldreich & Kwan 1974). Scenario (iii), where the [C II] and CO(1–0) optical depths are in the same regime is thus the only one that can fit the observed ratios, but only for excitation temperatures $\gtrsim$ 180 K. While we cannot distinguish mathematically between low and high optical depth, the known $\tau_{\mathrm{CO}(1-0)}$=1–10 and the equality of both the excitation temperatures and opacities would imply that also [C II] would need to be (nearly or fully) optically thick.

The only way the above scenario (iii) can fit the observed $L_{[\mathrm{C\,II}]}/L_{\mathrm{CO}(1-0)}$ ratio is in a thermalized region where both [C II] and CO(1–0) have excitation temperatures $\gtrsim$180 K (see Fig. 9). However, the average CO excitation temperatures in the SPT sample are $\lesssim$50 K (Spilker et al. 2014), well below the values required to fit the observed ratio (Fig. 9). The only way to reconcile the model in equation (2) with the known physical parameters of the CO ($\tau_{\mathrm{CO}(1-0)} > 1$ and $T_{\mathrm{ex,\,CO}} \lesssim 50$ K) is to allow for different excitation temperatures of [C II] and CO. Such different excitation temperatures also imply different [C II] and CO emitting regions within the GMCs.

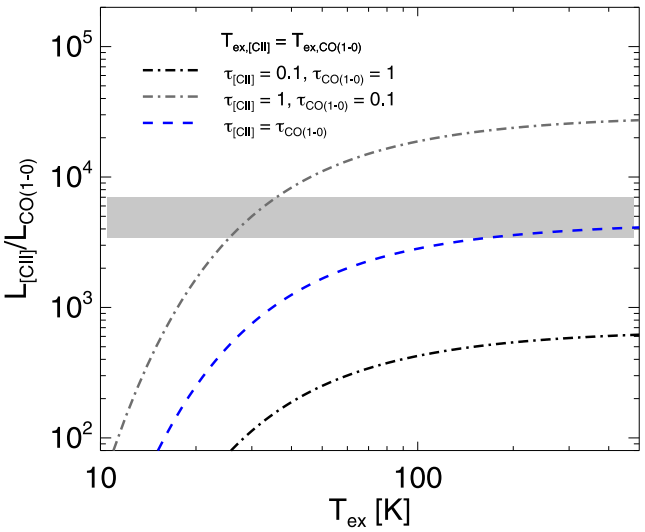

Figure 9. The $L_{[\mathrm{C\,II}]}/L_{\mathrm{CO}(1-0)}$ ratio predicted from the source functions versus equal [C II] and CO(1–0) excitation temperatures ($T_{\mathrm{ex},[\mathrm{C\,II}]} = T_{\mathrm{ex,\,CO}(1-0)}$), for three different cases of the optical depth: (i) optically thin [C II] and optically thick CO(1–0) (the black dot–dashed curve), (ii) optically thick [C II] and optically thin CO(1–0) – (the grey dot–dashed curve), (iii) same optical depth of [C II] and CO(1–0) (blue dashed curve). The grey shaded area represents the 1σ spread of the $L_{[\mathrm{C\,II}]}/L_{\mathrm{CO}(1-0)}$ ratio in the SPT sample. Case (i) underpredicts the ratio by an order of magnitude. Cases (ii) and (iii) can both reproduce the observed ratio. However, we know from ^{12}CO to ^{13}CO ratios that CO is optically thick (e.g. Spilker et al. 2014), which rules out case (ii). Only case (iii), implying optically thick CO and [C II], is consistent with all observational data.

5.1.3 *Different [C II] and CO excitation temperatures*

To examine the model from equation (2) with different excitation temperatures, we have to fix the observed $L_{[\mathrm{C\,II}]}/L_{\mathrm{CO}(1-0)}$ ratio and at least two parameters (two optical depths or an optical depths and a temperature). We first consider the case when $\tau_{[\mathrm{C\,II}]} = \tau_{\mathrm{CO}(1-0)}$, and plot $T_{\mathrm{ex,\,CO}(1-0)}$ as a function of $T_{\mathrm{ex},[\mathrm{C\,II}]}$ in Fig. 10 (blue dashed line with grey shaded area illustrating the observed $L_{[\mathrm{C\,II}]}/L_{\mathrm{CO}(1-0)}$ range). We conclude that $T_{\mathrm{ex},[\mathrm{C\,II}]} > T_{\mathrm{ex,\,CO}(1-0)}$ throughout. In the optically thick case, we can also allow for $1 \leq \tau_{[\mathrm{C\,II}]} < \tau_{\mathrm{CO}(1-0)}$. The red curve in Fig. 10 illustrates this for $\tau_{\mathrm{CO}(1-0)}$=4. Any further increase of the difference between $\tau_{[\mathrm{C\,II}]}$ and $\tau_{\mathrm{CO}(1-0)}$, will also increase the difference in T_{ex}. We warn that once both the [C II] and CO become strongly optically thick (i.e. $1 \ll \tau_{[\mathrm{C\,II}]} < \tau_{\mathrm{CO}(1-0)}$), one can no longer determine any differences between the optical depths, and hence no longer determine $T_{\mathrm{ex},[\mathrm{C\,II}]}$.

Alternatively, we can also fix the CO opacity and excitation temperature based on existing observations of the SPT DSFG sample, and determine which $T_{\mathrm{ex},[\mathrm{C\,II}]}$ values are predicted for a given $\tau_{[\mathrm{C\,II}]}$. Assuming the molecular gas is traced by CO(1–0) and the dust is thermalized allows us to fix the $T_{\mathrm{ex,\,CO}(1-0)} = T_{\mathrm{d}} \simeq 35$ K (Weiß et al. 2013). This value is consistent with the T_{kin} determined from the stacked ALMA spectrum of the SPT sample (Spilker et al. 2014). This $T_{\mathrm{ex,\,CO}(1-0)} = 5$ K case is illustrated in Fig. 11. If $\tau_{[\mathrm{C\,II}]} = \tau_{\mathrm{CO}(1-0)}$, this would imply $T_{\mathrm{ex},[\mathrm{C\,II}]} \sim 60 - 90$ K. Raising $\tau_{\mathrm{CO}(1-0)} = 4$ while keeping $\tau_{[\mathrm{C\,II}]} = 1$ would imply

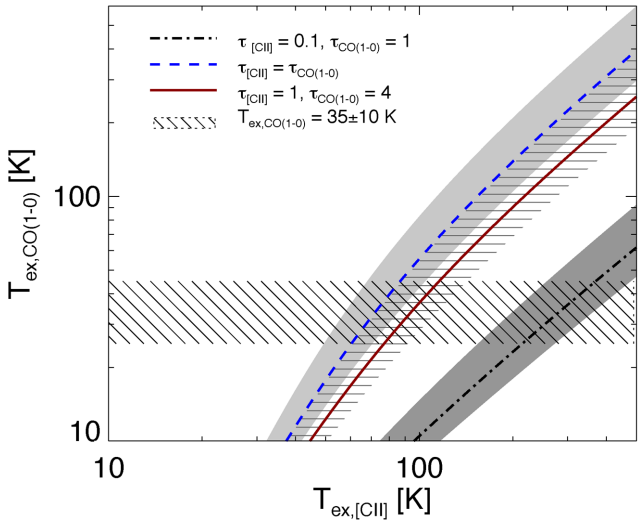

Figure 10. $T_{\rm ex,\,CO(1–0)}$ as a function of $T_{\rm ex,[C\,II]}$. In all cases, the excitation temperature of [C II] is higher than for CO(1–0). The blue dashed curve with the light grey shaded area shows the observed $L_{\rm [C\,II]}/L_{\rm CO(1-0)}$ =5200 ± 1800 range of SPT DSFGs in the case of equal [C II] and CO optical depths. The red continuous curve and hashed area illustrates that the difference between the excitation temperatures becomes even more significant for $\tau_{\rm [C\,II]}$=1 and $\tau_{\rm CO(1–0)}$= 4. The dot–dashed curve and the dark grey shaded area illustrate the case of $\tau_{\rm [C\,II]}$=0.1 and $\tau_{\rm CO(1–0)}$=1. The hashed horizontal area marks $T_{\rm ex,\,CO(1–0)}$=35 ± 10 K.

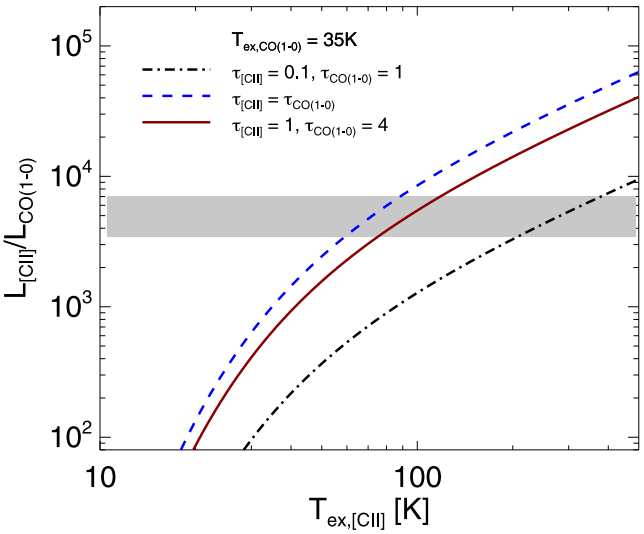

Figure 11. The $L_{\rm [C\,II]}/L_{\rm CO(1–0)}$ ratio as a function of the [C II] excitation temperature for a fixed $T_{\rm ex,\,CO(1–0)}$=35 K. The observed $L_{\rm [C\,II]}/L_{\rm CO(1–0)}$ ratio in the SPT DSFG sources (grey shaded area) is achieved within $T_{\rm ex,[C\,II]}$ ∼60–90 K for equal [C II] and CO optical depth (blue curve). In the case of $\tau_{\rm [C\,II]}$ =1 and $\tau_{\rm CO(1–0)}$ =4, the $L_{\rm [C\,II]}/L_{\rm CO(1–0)}$ ratio is achieved for $T_{\rm ex,[C\,II]}$ =85–110 K. The optically thin $\tau_{\rm [C\,II]}$ =0.1 and nearly optically thick $\tau_{\rm CO(1–0)}$ =1 case is reached by [C II] excitation temperatures in the range ∼240–330 K (black dashed curve).

$T_{\rm ex,[C\,II]}$ ∼80–110 K. The observed $L_{\rm [C\,II]}/L_{\rm CO(1–0)}$ ratios can also be reproduced with optically thin [C II] and (nearly) optically thick CO ($\tau_{\rm [C\,II]} = 0.1$ and $\tau_{\rm CO(1–0)} = 1$) when the [C II] excitation temperatures are ∼240–330 K. A determination of $T_{\rm ex,[C\,II]}$ is therefore needed to determine $\tau_{\rm [C\,II]}$. If the gas densities are higher than the critical density for [C II] (2400–6100 cm^{-3} for the above range of $T_{\rm ex,[C\,II]}$; Goldsmith et al. 2012), $T_{\rm ex,[C\,II]} \sim T$(gas). The gas temperatures can be obtained from observed [C II]/[OI] ratios (e.g. Stacey et al. 1983; Lord et al. 1996; Brauher et al. 2008), inferred through the peak [C II] antenna temperatures (e.g. Graf et al. 2012; Ossenkopf et al. 2013), or by theoretical modelling (e.g. Kaufman et al. 1999). These studies obtain T(gas) = 100−500 K, which from Fig. 11 would imply [C II] optical depths ranging from 0.1 to 1. However, the densities we derive from a comparison with PDR models (see Section 5.2.1) are in the range 100–10^5 (Table 2), with half of our sources below the [C II] critical density, so the $T_{\rm ex,[C\,II]} \sim T$(gas) may not be valid for a significant part of our sample. Hence, optical depths of $0.1 < \tau < 1$ are consistent with the observed line ratios in the SPT DSFG sample.

Table 2. The first column contains the names of the sources for which both [C II] and low-J CO lines have been detected. The second and third columns list G_0 and n for the sources determined from the PDR models in Fig. 12. Note that especially n can be very uncertain as the models are very degenerate in this part of the diagram. Column four gives the size range determined using the short and long mean free path assumed by Stacey et al. (2010). The fifth column lists the radii for the sources which have lens models (Hezaveh et al. 2013), and the sixth column gives the range in sizes of the molecular gas estimated from the molecular gas mass range given by $\alpha_{\rm CO} = (0.8–2)\,{\rm M}_\odot$ (K km s^{-1} pc^2)$^{-1}$. The last column lists the lensing magnification factor from Hezaveh et al. (2013); SPT0529-54 is not included in this table as low-J CO lines have not been observed for this source. The sources marked with †, we have assumed a mean of $\langle\mu\rangle = 14.1$ (see Section 3.2).

Source	G_0	n (cm^{-3})	R(PDR) (kpc)	R$_{1/2}$(lens model) (kpc)	R($L'_{\rm CO(1-0)}$) (kpc)	μ
SPT0113-46	10^3	10^3	0.6–1.1	–	0.85 − 1.16	–†
SPT0345-47	10^4	5×10^4	0.4–0.7	–	0.39 − 0.52	–†
SPT0346-52	8×10^3	10^5	0.7–1.5	0.59 ± 0.03	0.18 − 0.24	5.4±0.2
SPT0243-49	5×10^3	10^3	0.4–0.6	–	0.85 − 1.15	–†
SPT0418-47	10^3	100	0.7–1.5	1.07 ± 0.17	2.26 − 3.07	21.0±3.5
SPT0441-46	8×10^3	10^4	0.3–0.5	–	0.36 − 0.49	–†
SPT2103-60	10^3	100	0.7–1.4	–	1.69 − 2.30	–†
SPT2146-55	5×10^3	10^4	0.5–0.8	–	0.42 − 0.56	–†
SPT2147-50	5×10^3	10^4	0.4–0.6	–	0.33 − 0.45	–†
SPT0551-50	10^2	100	1.0–2.6	–	1.40 − 1.89	–†
SPT0538-50	10^2	100	1.7–5.9	1.07 ± 0.25	2.46 − 3.34	20.9 ± 4.2

We also compare the model predictions in Fig. 11 with the low- and high-z comparison samples. The lower average $L_{[C\,II]}/L_{CO(1-0)}$ ratios in these samples (though with a much larger spread than for the SPT DSFGs) imply $T_{ex,[C\,II]}$ between ∼30 and ∼200 K. In particular for the low-z sample, optically thick [C II] and CO emission would imply very low $T_{ex,[C\,II]}$ ∼40 K, well below the ground state energy. The difference between the SPT DSFG and the low-z comparison sample could therefore be ascribed to a lower optical depths in the nearby sources. In the context of PDR models, this can also be understood as a decrease of the G_0/n ratio. Reducing this parameter implies smaller [C II] emitting columns and a smaller effective optical depth. The lower G_0/n ratio in the low-z sample could be an effect of the lower FUV fields found in galaxies forming stars at a more modest rate (Stacey et al. 1991a, 1993; Kaufman et al. 1999).

Finally, we note that Fig. 8 also contains some low-z sources with $L_{[C\,II]}/L_{CO(1-0)}$ ratios >15 000. Such values are difficult to explain with standard PDR models. Low metallicity has been invoked to explain these sources (e.g. Maloney & Black 1988; Stacey et al. 1991a; Madden et al. 1997). Considering this effect is beyond the scope of this paper.

In summary, the observed $L_{[C\,II]}/L_{CO(1-0)}$ ratios in the SPT DSFGs are best described by a non-uniform medium of [C II] and CO(1–0) emitting gas with $T_{ex,[C\,II]} > T_{ex,\,CO(1-0)}$, $\tau_{CO(1-0)} \gg 1$ and $\tau_{[C\,II]} \lesssim 1$.

5.2 Implications of different [C II] and CO(1–0) excitation temperatures

In Section 5.1.2, we concluded that a homogeneous region with thermalized CO and [C II] gas is incompatible with the observed $L_{[C\,II]}/L_{CO(1-0)}$ ratios. Even in the optically thick case, the only way to reproduce the observed ratio is for higher [C II] than CO(1–0) excitation temperatures (see Fig. 10). The cases of uniform and separated [C II] and CO gas was recently studied by Mashian, Sternberg & Loeb (2013). They explore four different models to explain the observations in the high-z submillimetre source HDF 850.1: (1) separate CO–[C II] virialized gas, (2) separate CO–[C II] unvirialized gas, (3) uniformly mixed CO–[C II] virialized gas and (4) uniformly mixed CO–[C II] unvirialized gas. Based on cosmological constraints due to the dark matter halo abundance in the standard Λ cold dark matter cosmology, they rule out three of the models and conclude that the preferred model is an unvirialized molecular cloud model with independent CO and [C II] emitting gas with an average kinetic temperature of 100 K and density of 10^3 cm^{-3} for the molecular gas. Both our conclusions and those of Mashian et al. (2013) are completely consistent with the structure described by PDR models.

PDRs are clouds of molecular gas associated with star-forming regions, as they are often found near young massive O and B stars, acting as the source of the FUV photons that determine the temperature and chemical composition of the gas (Meijerink et al. 2007). Schematically, in a PDR the increasing extinction (A_V) with depth into the cloud creates a layer structure, where the surface of the cloud with $A_V \sim 1$ is dominated by H^+, C^+, and O I. As the gas becomes more self-shielded against the dissociating FUV photons deeper in ($A_V \sim$ 2–4), layers of H I and H_2 form and a transition region of C^+, C, and CO is present. At the centre of the cloud, the molecular gas is so opaque that the chemistry and heating are dominated by cosmic rays. Hence, the [C II] fine structure line probes the surface of a PDR where $A_V \lesssim 1$ and $T \gtrsim 100$ K, while CO traces the core of the cloud. To derive detailed physical parameters from the PDR models therefore requires spatially resolved observations of different species such as C, C^+, CO, O, H_2, polycyclic aromatic hydrocarbons and dust continuum emission (e.g. Hollenbach & Tielens 1999; Orr, Pineda & Goldsmith 2014).

5.2.1 *Implications of the PDR structure*

The structure of the gas in PDRs allows for different [C II] and CO(1–0) excitation temperatures. The physical parameters for the ISM in low- and high-z galaxies predicted by basic PDR models can be compared with observed data in a diagnostic diagram (Fig. 12) first presented by Wolfire et al. (1989) and updated by e.g. Stacey et al. (1991a, 2010) and Hailey-Dunsheath et al. (2010). The diagram has the advantage of plotting ratios where the lensing magnification factors for high-z sources, beam-filling factors for low-z sources and filling factors for the PDRs (which are unknown, but assumed the same for [C II] and CO(1–0)) are divided out. It can be used to roughly estimate the strength of the FUV field and the gas density. One has to be cautious using this diagram, as the FIR luminosity can contain strong contributions from other sources not associated with PDRs (e.g. AGN tori).

The SPT sample is ideal in this respect as [C II] has been measured for 17 out of 20, and low-J CO for 11 (see Table 1) of these sources, so the CO luminosities for our sources (unlike the comparison samples) do not depend on uncertain scaling factors. The SPT sample is the most complete high-z sample included in this diagram. The comparison sample is also integrated over entire galaxies enabling a fair comparison to the SPT sample.

The PDR model used in this diagram (Kaufman et al. 1999) models a plane-parallel slab divided into a number of zones of different depths. The intensities are modelled for a parameter space of the FUV field strength (G_0) in units of the local Galactic interstellar radiation field (the 'Habing Field', 1.6×10^{-3} ergs cm^{-3}s^{-1}; Kaufman et al. 1999) in the range $10^{-0.5} \leq G_0 \leq 10^{6.5}$ and the gas densities in the range 10 cm$^{-3} \leq n \leq 10^7$ cm^{-3}. The emission from different species depends on the density, the field strength, and the depth into the cloud. Hailey-Dunsheath et al. (2010) assume that 70 per cent of the [C II] emission originates from PDRs (see also Section 5.2.2), meaning that the points would move slightly down in Fig. 12 if this was corrected for.

By comparing the SPT data points with the PDR model tracks in Fig. 12, we obtain a rough estimate of the radiation field strength and the gas density of $100 < G_0 < 8000$ and 10^2 cm^{-3} $< n < 10^5$ cm^{-3} (see Table 2). These values are consistent with the ones found in previous samples of DSFGs (e.g. Stacey et al. 2010). They imply PDR surface temperatures of 300–500 K (fig. 2 of Kaufman et al. 1999). As these surface temperatures are representative for regions up to $A_V \sim 2$, they cover most of the [C II] emitting region. They are consistent with other derivations of the gas temperatures (see Section 5.1.3). If the density exceeds the [C II] critical density, these temperatures also represent $T_{ex,[C\,II]}$, which would imply optically thin [C II] (Fig. 11). However, in half of our sources, the densities are below the critical densities, so a range of opacities up to unity remains possible.

Sizes of PDRs Comparing the L_{FIR}/μ for the SPT sources,[11] which lie in the range $(1.1–21.9)\mu^{-1} \times 10^{12}$ L$_\odot$, with the local starburst galaxy M82 (L_{FIR}∼(2.3–3.2) × 10^{10} L$_\odot$; Rice et al. 1988 and Colbert et al. 1999) show the significant difference in L_{FIR} at high and

[11] See Section 3.2 for a discussion on the lensing magnification factor μ in our sample.

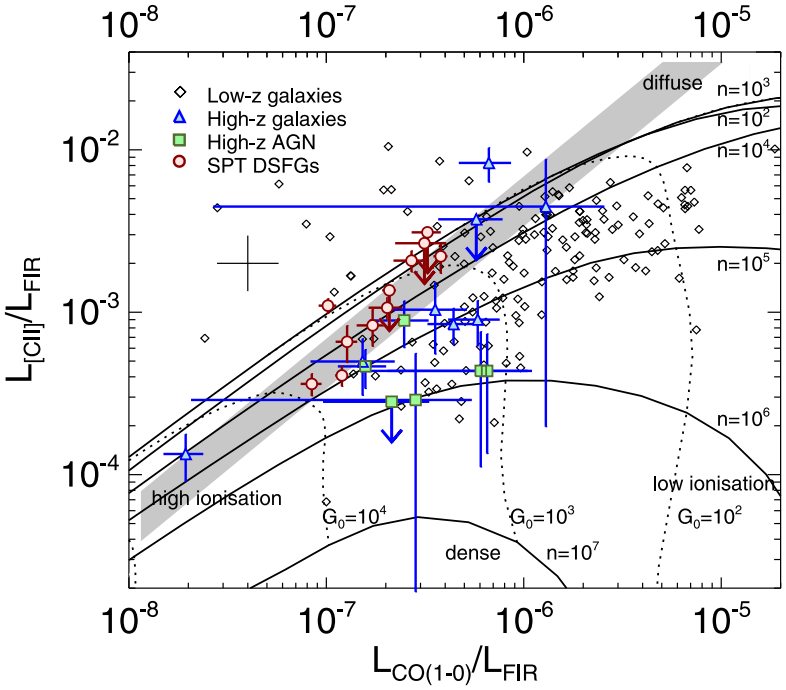

Figure 12. $L_{[\mathrm{C\,II}]}/L_{\mathrm{FIR}}$ versus $L_{\mathrm{CO(1-0)}}/L_{\mathrm{FIR}}$ for the SPT sources and the low- and high-z comparison sample. The figure (e.g. Wolfire et al. 1989; Stacey et al. 2010) compares the values of the strength of the radiation field G_0 and the density n for low- and high-z sources. The diagram is independent of lensing magnification factors for high-z source and beam filling factors for low-z sources as both the [C II] and CO(1–0) emission is normalized by the FIR luminosity. The typical error bar is represented by the black cross. To compare the observations with the model contours, Stacey et al. (2010) assume that 70 per cent of the [C II] emission originate from PDRs. The grey shaded area represents the 1σ spread of the $L_{[\mathrm{C\,II}]}/L_{\mathrm{CO(1-0)}}$ ratio in the SPT sample.

low redshifts. Using this comparison and estimates of G_0 for each SPT DSFG, we estimate approximate sizes of the PDRs populating the galaxies, following Stacey et al. (2010). For this, we assume the molecular clouds are randomly mixed with young stellar clusters, acting as the radiation sources, within the galaxy (Wolfire, Tielens & Hollenbach 1990). Assuming this structure, the relationship between the average G_0, the total size of the PDRs (D, diameter), and the total luminosity (L_{FIR}) of the source is given by $G_0 \propto \lambda L_{\mathrm{FIR}}/D^3$ for a short mean free path (λ) and $G_0 \propto L_{\mathrm{FIR}}/D^2$ for large mean free path of the FUV photons (see Wolfire et al. 1990). To estimate the approximate sizes, we read off G_0 and L_{FIR} for the SPT DSFGs from Fig. 12, and scale these with the values obtained for M82 ($G_0 \sim 1000$; Lord et al. 1996, $L_{\mathrm{FIR}} \sim 2.8 \times 10^{10}$ $\mathrm{L}_\odot$, average of the values determined by Rice et al. 1988 and Colbert et al. 1999), assuming the same mean free path for the SPT sources and M82. The exact size of the PDR region in M82 is rather uncertain with reported sizes ranging from 300 pc (Joy, Lester & Harvey 1987) to 600 pc (Carlstrom & Kronberg 1991). For consistency with Stacey et al. (2010), we will assume $D \sim 300$ pc. We warn that differential lensing (if significant, see Section 3.2) could affect the positions of the sources in Fig. 12 leading to different estimations of G_0 and therewith the sizes. The radii we estimate are listed in Table 2, along with our estimated G_0 and n. An estimate of the source radii from lens modelling is available for four sources in Table 2. The estimated radii of the PDRs, while fairly uncertain, are comparable to the source sizes determined by the lens models.

A rough estimate of the size ranges occupied by the molecular gas is given in Table 2 as well. These sizes are estimated using the molecular gas mass estimated from $L'_{\mathrm{CO(1-0)}}$. Using low and high CO-to-H_2 conversion factors often used in the literature of $\alpha_{\mathrm{CO}} = 0.8\,\mathrm{M}_\odot\,(\mathrm{K\ km\ s^{-1}\ pc^2})^{-1}$ (see Section 4.2, Downes & Solomon (1998)) and $\alpha_{\mathrm{CO}} = 2\,\mathrm{M}_\odot\,(\mathrm{K\ km\ s^{-1}\ pc^{-2}})^{-1}$ (e.g. Swinbank et al. 2011), we estimate sizes of the molecular gas regions making the simplistic assumption that the gas is uniformly distributed in a sphere with radius R and density n as listed in Table 2. The sizes estimated using this method are quite uncertain as we do not take into account non-uniform density profiles or non-unity volume filling factors of the gas. They are roughly consistent with both the sizes obtained from the PDR model, and the more accurate sizes derived from the lens models. We note that these kpc-scales are close to the typical sizes of host galaxies, and could be easily spatially resolved, especially given the lensing magnification, allowing detailed future studies of their spatial distributions.

5.2.2 *Other contributions to the [C II] emission*

The [C II] emission integrated over an entire galaxy will contain contributions from regions with different physical conditions such as XDRs, CRDRs, shock-dominated regions, diffuse warm gas, H II regions, and PDRs. Above, we have assumed that observed [C II] emission in the SPT DSFGs is dominated by emission from PDRs on molecular cloud surfaces (e.g. Stutzki et al. 1988; Stacey et al. 1993). We now consider the possible contributions from the alternative [C II]-emitting regions in increasing order of importance.

In the vicinity of an AGN, supplying X-ray radiation, we expect XDRs. X-ray photons penetrate deeper into the volume of the interstellar clouds than the FUV photons in PDRs as the absorption cross-sections are smaller for X-ray energies. As argued in Sections 4.1.3 and 4.4, the SPT sample does not show evidence for strong AGN activity, and XDR contributions are therefore expected to be negligible.

In CRDRs, the gas heating and chemistry are controlled through interactions with high-energy particles. As the energy density in cosmic rays is low compared to photons, CRDRs are thought to trace the dense, innermost regions of GMCs, rather than the outer surfaces where [C II] emission is assumed to be more prevalent (Viti et al. 2013). We therefore assume the CRDR contribution to be negligible.

Turbulence and shocks have been suggested by Appleton et al. (2013) to be an additional source of [C II] emission. They suggest that this mechanism should be present in highly turbulent conditions such as colliding galaxies and the early stages of galaxy–disc build up. However, for low turbulent velocities, it becomes difficult to distinguish between this mechanism and low-density PDRs. The extreme $L_{[\mathrm{C\,II}]}/L_{\mathrm{FIR}}$ ratios Appleton et al. (2013) find for the intergalactic filament in Stephan's Quintet are ∼30 times higher than those observed in the SPT sample. Smaller shock-ionized regions may still contribute significantly to the observed [C II] emission. However, it would be difficult to explain the relatively narrow spread in the observed [C II] to CO ratio if a range of such shock-ionized regions would be a frequent occurrence in our SPT sources. We therefore do not expect this mechanism to be important in our samples.

The [C II] emission could also originate from the diffuse warm low-density medium in between the GMCs. Spatially resolved [C II] and CO observations are required to differentiate between the PDR and diffuse components. Observations of another lensed DSFGs, HLSJ091828.6+514223 at $z = 5.243$ (Rawle et al. 2014), do show that the [C II] and CO(1–0) have a consistent structure and velocity profile, though the resolution may not go down to the scales of the GMCs (a few hundred pc). Observations of [C II] and CO at spatial resolutions of ∼50 mas are required to constrain this diffuse component in our DFSGs.

H II regions surround young O and B stars which emit Lyman continuum photons with energies exceeding the ionization energy of hydrogren (13.6 eV). Abel (2006) explore the contribution of [C II] emission from H II regions for a wide range in temperature, ionization parameter (U) and electron density, and find that at least 10 per cent, and sometimes up to 50–60 per cent of the total [C II] emission comes from within the H II regions. Observations of other fine structure lines that only trace H II regions are required to determine the exact contribution from H II regions. Oberst et al. (2006, 2011) used the observed [C II]/[N II] 205 μm ratio in the Carina nebula to constrain the contribution from H II regions to 30 per cent. This technique has since also been applied to high-redshift objects (Ferkinhoff et al. 2011; Decarli et al. 2014).

5.3 The [C II]/FIR luminosity deficit

Several studies have reported a 'deficit' in the ratio of the [C II] line strength to the FIR luminosity ratio ($L_{[\mathrm{C\,II}]}/L_{\mathrm{FIR}}$) for LIRGs with $L_{\mathrm{FIR}} \gtrsim 10^{11}$ L$_\odot$ (e.g. Malhotra et al. 1997, Luhman et al. 1998, Maiolino et al. 2009; Stacey et al. 2010; Graciá-Carpio et al. 2011; Sargsyan et al. 2012). Various physical explanations for this trend have been proposed, including an increased ionization parameter (Malhotra et al. 2001; Abel et al. 2009; Graciá-Carpio et al. 2011), collisional de-excitation of [C II] (Appleton et al. 2013) and non-PDR contributions to the FIR luminosity (Luhman et al. 2003), possibly from AGN (Sargsyan et al. 2012).

Stacey et al. (2010) argued that the lower [C II]/FIR ratio can be explained by the fact that the star formation in local ULIRGs is confined and vigorous (leading to high G_0), while in the most distant objects, the star formation is very large scale, but of lower intensity (i.e. lower G_0). In PDR models, the [C II]/FIR ratio is inversely proportional with G_0. Contrary to the FIR luminosity, which scales linearly with G_0, the [C II] luminosity increases only slowly with G_0. This is because in the observed density regime, the C^+ column density scales only with dust extinction, while the emissivity is only weakly dependent on G_0 since the gas temperature is above the excitation potential of 92 K. This leads to a 'saturation effect' of the [C II] emission at high luminosity in nearby ULIRGs, while the FIR remains unsaturated. This is consistent with a recent study by Díaz-Santos et al. (2014) exploring the difference in the [C II]/FIR luminosity deficit between the extended and compact (nuclei) regions in nearby LIRGs, revealing a larger deficit in the [C II]/FIR luminosity ratio for the compact regions than for the extended regions. The 'deficit' is mostly confined to the innermost compact regions, while [C II] to FIR luminosity ratio for the extended regions is similar to that found in the extended discs of normal star-forming galaxies.

A similar saturation effect would also occur when the [C II] line becomes (nearly) optically thick. The line then reaches its maximum brightness, in the sense that any additional incoming ionizing photons will not increase the brightness of the line further. However, the cooling of these additional ionizing photons may still continue through optically thin processes, notably the dust continuum. An alternative or additional way of decreasing the [C II] to FIR luminosity ratio is therefore to have optically thick [C II] and optically thin dust continuum emission. The higher density in the more compact regions may then increase the probability of the [C II] to become optically thick.

Finally, we note that the [C II] to FIR 'deficit' at high luminosities is also reported for other fine structure lines such as [O I], [O III], [N II], and [N III], indicating that this 'deficit' is a general aspect of all FIR fine structure lines, regardless of their origin in the ionized or neutral phase of the ISM (e.g. Graciá-Carpio et al. 2011; Farrah et al. 2013).

6 CONCLUSIONS

We have presented the first uniformly selected [C II] survey of lensed DSFGs covering the redshift range $z = 2.1$–5.7. We have detected [C II] for 17 out of 20 sources, 11 of which are also observed and detected in low-J CO lines. This sample facilitates statistical studies of the ISM at high redshift. Our main results and conclusions are as follows.

(1) We fit single or double Gaussian functions to the CO and [C II] velocity profiles, and find consistent velocity profiles in 13 out of 14 CO detections with ALMA. This suggest that differential lensing is not significant in these cases, and is consistent with the idea that the [C II] and CO(1–0) emitting gas are spatially associated.

(2) The line luminosity ratio of the [C II] and CO(1–0) detections for the SPT sources is $\sim 5200 \pm 1800$, which agrees with the first reported ratio by Crawford et al. (1985). The values derived from the SPT sample are consistent with both low-z and high-z comparison samples, but with significantly smaller dispersion. This is presumably due to the homogeneity of the SPT selection and follow-up observations and absence of any known AGN-dominated sources, which have lower [C II] to CO(1–0) ratios.

(3) The SPT sample covers the same spread in the $L_{[\mathrm{C\,II}]}/L_{\mathrm{FIR}}$ ratio as the $L_{\mathrm{FIR}} \gtrsim 10^{11}$ L$_\odot$ sources in both our low-z and high-z comparison samples. AGN-dominated sources increase the scatter towards lower $L_{[\mathrm{C\,II}]}/L_{\mathrm{FIR}}$ ratios in the comparison sample.

(4) We investigate the origin of the [C II] emission using the observed $L_{[\mathrm{C\,II}]}/L_{\mathrm{CO(1-0)}}$ ratio, and conclude that the observed ratio

is best described by a medium of [C II] and CO(1–0) emitting gas with $T_{\rm ex,[C\,II]} > T_{\rm ex,\,CO(1-0)}$, optically thick CO ($\tau_{\rm CO(1-0)} > 1$), and low to moderate [C II] optical depth ($\tau_{\rm [C\,II]} \lesssim 1$). The structure of PDRs allows for such different excitation temperatures of the [C II] and CO(1–0) emitting gas. Interestingly, the PDR models converge to this [C II] to CO(1–0) ratio for densities below 10^5 cm^{-3}.

(5) We revisit the $L_{\rm [C\,II]}/L_{\rm FIR}$ 'deficit' observed for sources with $L_{\rm FIR} \gtrsim 10^{11}$ L$_\odot$, which has been explained as a 'saturation effect' of the [C II] emission in compact regions with higher G_0 factors. An alternative or additional explanation for this saturation effect is (nearly) optically thick [C II] emission. In this case, the [C II] line becomes saturated and reaches the maximum [C II] brightness, while cooling via the FIR continuum emission continues. The variation in the $L_{\rm [C\,II]}/L_{\rm FIR}$ ratio is therefore dominated by the variation in $L_{\rm FIR}$ rather than $L_{\rm [C\,II]}$.

(6) We determine the FIR luminosity for both the SPT sample and the comparison low- and high-z sample in a consistent way, adding 11 SPT DSFGs to the $L_{\rm [C\,II]}/L_{\rm FIR}$ versus $L_{\rm CO(1-0)}/L_{\rm FIR}$ plot in Fig. 12. We compare the SPT sample with PDR models and estimate the radiation field strength and average gas density to be in the range $100 < G_0 < 8000$ and 10^2 cm^{-3} $< n < 10^5$ cm^{-3}.

The reliability of [C II] as a tracer of star formation rate (SFR) has been explored by e.g. De Looze et al. (2014). They show that [C II] is a good tracer for the SFR except for low-metallicity sources. Determining the metallicity using other fine structure lines such as [N II], [O II], and [O III], and the contribution to the [C II] emission from H II regions (Croxall et al. 2012) are therefore key in finding the most reliable tracer of SFR in nearby and distant galaxies. Thus far, all high-z fine structure line measurements have been unresolved, but thanks to lens shear of gravitationally lensed sources it will become possible to resolve structures down to 100 pc scales (Swinbank et al. 2010). Hence, for PDRs of the sizes estimated here, future observations with ALMA will be able to spatially resolve [C II] emission and other fine structure lines and provide new insight into how [C II] emission traces gas.

ACKNOWLEDGEMENTS

We thank the referee for a very thorough reading of the paper and constructive comments which have significantly improved the paper. We are grateful to Javier Gracia-Carpio for providing us with a sample of low- and high-z sources with both [C II] and CO detections, ideal for comparison with the SPT sample of high-z sources. We also thank Gordon Stacey and Padelis Papadopoulos for lively, educational, and profitable discussions. We thank Göran Pilbratt, *Herschel* Project scientist for the allocated *Herschel* SPIRE Directors Discretionary Time and Richard George and Ivan Valtchanov for helpful comments on the *Herschel* SPIRE FTS data reduction.

This publication is based on data acquired with the APEX. APEX is a collaboration between the Max-Planck-Institut fur Radioastronomie, the European Southern Observatory, and the Onsala Space Observatory. This paper makes use of the following ALMA data: ADS/JAO.ALMA#2011.0.00957.S, ADS/JAO.ALMA#2011.0.00958.S and ADS/JAO.ALMA#2012.1.00844.S. ALMA is a partnership of ESO (representing its member states), NSF (USA) and NINS (Japan), together with NRC (Canada) and NSC and ASIAA (Taiwan), in cooperation with Republic of Chile. The Joint ALMA Observatory is operated by ESO, AUI/NRAO and NAOJ. The ATCA is part of the Australia Telescope National Facility which is funded by the Commonwealth of Australia for operation as a National Facility managed by CSIRO. This research has made use of the NED which is operated by the Jet Propulsion Laboratory, California Institute of Technology, under contract with the National Aeronautics and Space Administration. This research has made use of NASA's Astrophysics Data System Bibliographic Services

This material is based on work supported by the US National Science Foundation under grant no. AST-1312950. The SPT is supported by the National Science Foundation through grant PLR-1248097. Partial support is also provided by the NSF Physics Frontier Center grant PHY-1125897 to the Kavli Institute of Cosmological Physics at the University of Chicago, the Kavli Foundation, and the Gordon and Betty Moore Foundation grant GBMF 947.

REFERENCES

Abel N. P., 2006, MNRAS, 368, 1949
Abel N. P., Dudley C., Fischer J., Satyapal S., van Hoof P. A. M., 2009, ApJ, 701, 1147
Appleton P. N. et al., 2013, ApJ, 777, 66
Aravena M. et al., 2008, A&A, 491, 173
Aravena M. et al., 2013, MNRAS, 433, 498
Aravena M. et al., 2014, MNRAS, 442, 558
Barger A. J., Cowie L. L., Sanders D. B., Fulton E., Taniguchi Y., Sato Y., Kawara K., Okuda H., 1998, Nature, 394, 248
Baugh C. M., Lacey C. G., Frenk C. S., Granato G. L., Silva L., Bressan A., Benson A. J., Cole S., 2005, MNRAS, 356, 1191
Benson A. J., 2012, New Astron., 17, 175
Boreiko R. T., Betz A. L., 1996, ApJ, 467, L113
Bothwell M. S. et al., 2013a, MNRAS, 429, 3047
Bothwell M. S. et al., 2013b, ApJ, 779, 67
Braine J. et al., 2012, A&A, 544, A55
Brauher J. R., Dale D. A., Helou G., 2008, ApJS, 178, 280
Brisbin D., Ferkinhoff C., Nikola T., Parshley S., Stacey G. J., Spoon H., Hailey-Dunsheath S., Verma A., 2015, ApJ, 799, 13
Carilli C. L., Walter F., 2013, ARA&A, 51, 105
Carilli C. L. et al., 2002a, AJ, 123, 1838
Carilli C. L. et al., 2002b, ApJ, 575, 145
Carlstrom J. E., Kronberg P. P., 1991, ApJ, 366, 422
Carlstrom J. E. et al., 2011, PASP, 123, 568
Casey C. M., Narayanan D., Cooray A., 2014, Phys. Rep., 541, 45
Chapman S. C., Blain A. W., Smail I., Ivison R. J., 2005, ApJ, 622, 772
Colbert J. W. et al., 1999, ApJ, 511, 721
Coppin K. E. K. et al., 2010, MNRAS, 407, L103
Cox P. et al., 2011, ApJ, 740, 63
Crawford M. K., Genzel R., Townes C. H., Watson D. M., 1985, ApJ, 291, 755
Crawford M. K., Lugten J. B., Fitelson W., Genzel R., Melnick G., 1986, ApJ, 303, L57
Croxall K. V. et al., 2012, ApJ, 747, 81
Dalgarno A., McCray R. A., 1972, ARA&A, 10, 375
De Breuck C., Maiolino R., Caselli P., Coppin K., Hailey-Dunsheath S., Nagao T., 2011, A&A, 530, L8
De Breuck C. et al., 2014, A&A, 565, A59
De Looze I. et al., 2014, A&A, 568, A62
Decarli R. et al., 2014, ApJ, 782, L17
Díaz-Santos T. et al., 2013, ApJ, 774, 68
Díaz-Santos T. et al., 2014, ApJ, 788, L17
Downes D., Solomon P. M., 1998, ApJ, 507, 615
Ellis H. B., Jr, Werner M. W., 1984, BAAS, 16, 463
Evans A. S., Sanders D. B., Mazzarella J. M., Solomon P. M., Downes D., Kramer C., Radford S. J. E., 1996, ApJ, 457, 658
Farrah D. et al., 2013, ApJ, 776, 38
Ferkinhoff C. et al., 2011, ApJ, 740, L29
Fixsen D. J., Bennett C. L., Mather J. C., 1999, ApJ, 526, 207
Frayer D. T. et al., 2008, ApJ, 680, L21
Frayer D. T. et al., 2011, ApJ, 726, L22
George R. D. et al., 2013, MNRAS, 436, L99

Goldreich P., Kwan J., 1974, ApJ, 189, 441
Goldsmith P. F., Langer W. D., Pineda J. L., Velusamy T., 2012, ApJS, 203, 13
Graciá-Carpio J. et al., 2011, ApJ, 728, L7
Graf U. U. et al., 2012, A&A, 542, L16
Greve T. R. et al., 2005, MNRAS, 359, 1165
Greve T. R. et al., 2012, ApJ, 756, 101
Griffin M. J. et al., 2010, A&A, 518, L3
Guilloteau S., Omont A., Cox P., McMahon R. G., Petitjean P., 1999, A&A, 349, 363
Hailey-Dunsheath S., Nikola T., Stacey G. J., Oberst T. E., Parshley S. C., Benford D. J., Staguhn J. G., Tucker C. E., 2010, ApJ, 714, L162
Hainline L. J., Blain A. W., Smail I., Alexander D. M., Armus L., Chapman S. C., Ivison R. J., 2011, ApJ, 740, 96
Hayward C. C., Narayanan D., Kereš D., Jonsson P., Hopkins P. F., Cox T. J., Hernquist L., 2013, MNRAS, 428, 2529
Helou G., Khan I. R., Malek L., Boehmer L., 1988, ApJS, 68, 151
Heyminck S., Kasemann C., Güsten R., de Lange G., Graf U. U., 2006, A&A, 454, L21
Hezaveh Y. D., Holder G. P., 2011, ApJ, 734, 52
Hezaveh Y. D., Marrone D. P., Holder G. P., 2012, ApJ, 761, 20
Hezaveh Y. D. et al., 2013, ApJ, 767, 132
Hollenbach D. J., Tielens A. G. G. M., 1999, Rev. Mod. Phys., 71, 173
Hughes D. H. et al., 1998, Nature, 394, 241
Huynh M. T. et al., 2014, MNRAS, 443, L54
Iono D. et al., 2006, ApJ, 645, L97
Ivison R. J. et al., 2010, A&A, 518, L35
Joy M., Lester D. F., Harvey P. M., 1987, ApJ, 319, 314
Kaufman M. J., Wolfire M. G., Hollenbach D. J., Luhman M. L., 1999, ApJ, 527, 795
Klein B., Philipp S. D., Krämer I., Kasemann C., Güsten R., Menten K. M., 2006, A&A, 454, L29
Komatsu E. et al., 2011, ApJS, 192, 18
Lacey C. G., Baugh C. M., Frenk C. S., Benson A. J., Orsi A., Silva L., Granato G. L., Bressan A., 2010, MNRAS, 405, 2
Lavalley M. P., Isobe T., Feigelson E. D., 1992, BAAS, 24, 839
Lord S. D., Hollenbach D. J., Haas M. R., Rubin R. H., Colgan S. W. J., Erickson E. F., 1996, ApJ, 465, 703
Luhman M. L. et al., 1998, ApJ, 504, L11
Luhman M. L., Satyapal S., Fischer J., Wolfire M. G., Sturm E., Dudley C. C., Lutz D., Genzel R., 2003, ApJ, 594, 758
Madden S., Geis N., Genzel R., Nikola T., Poglitsch A., Stacey G. J., Townes C., 1997, in Wilson A., ed., ESA Special Publ., Vol. 401, The Far Infrared and Submillimetre Universe. ESA, Noordwijk, p. 111
Maiolino R. et al., 2005, A&A, 440, L51
Maiolino R., Caselli P., Nagao T., Walmsley M., De Breuck C., Meneghetti M., 2009, A&A, 500, L1
Malhotra S. et al., 1997, ApJ, 491, L27
Malhotra S. et al., 2001, ApJ, 561, 766
Maloney P., Black J. H., 1988, ApJ, 325, 389
Mashian N., Sternberg A., Loeb A., 2013, MNRAS, 435, 2407
Meijerink R., Spaans M., Israel F. P., 2007, A&A, 461, 793
Michałowski M. J., Dunlop J. S., Cirasuolo M., Hjorth J., Hayward C. C., Watson D., 2012, A&A, 541, A85
Mittal R. et al., 2011, MNRAS, 418, 2386
Mocanu L. M. et al., 2013, ApJ, 779, 61
Negishi T., Onaka T., Chan K.-W., Roellig T. L., 2001, A&A, 375, 566
Neri R., Downes D., Cox P., Walter F., 2014, A&A, 562, A35
Oberst T. E. et al., 2006, ApJ, 652, L125
Oberst T. E., Parshley S. C., Nikola T., Stacey G. J., Löhr A., Lane A. P., Stark A. A., Kamenetzky J., 2011, ApJ, 739, 100
Orr M. E., Pineda J. L., Goldsmith P. F., 2014, ApJ, 795, 26
Ossenkopf V., Röllig M., Neufeld D. A., Pilleri P., Lis D. C., Fuente A., van der Tak F. F. S., Bergin E., 2013, A&A, 550, A57
Penzias A. A., Solomon P. M., Jefferts K. B., Wilson R. W., 1972, ApJ, 174, L43
Pilbratt G. L. et al., 2010, A&A, 518, L1
Rawle T. D. et al., 2014, ApJ, 783, 59
Rice W., Lonsdale C. J., Soifer B. T., Neugebauer G., Kopan E. L., Lloyd L. A., de Jong T., Habing H. J., 1988, ApJS, 68, 91
Riechers D. A. et al., 2013, Nature, 496, 329
Sargsyan L. et al., 2012, ApJ, 755, 171
Sargsyan L., Samsonyan A., Lebouteiller V., Weedman D., Barry D., Bernard-Salas J., Houck J., Spoon H., 2014, ApJ, 790, 15
Smail I., Ivison R. J., Blain A. W., 1997, ApJ, 490, L5
Solomon P. M., Vanden Bout P. A., 2005, ARA&A, 43, 677
Spilker J. S. et al., 2014, ApJ, 785, 149
Stacey G. J., Smyers S. D., Kurtz N. T., Harwit M., 1983, ApJ, 265, L7
Stacey G. J., Geis N., Genzel R., Lugten J. B., Poglitsch A., Sternberg A., Townes C. H., 1991a, ApJ, 373, 423
Stacey G. J., Townes C. H., Geis N., Madden S. C., Herrmann F., Genzel R., Poglitsch A., Jackson J. M., 1991b, ApJ, 382, L37
Stacey G. J., Jaffe D. T., Geis N., Grenzel R., Harris A. I., Poglitsch A., Stutzki J., Townes C. H., 1993, ApJ, 404, 219
Stacey G. J., Hailey-Dunsheath S., Ferkinhoff C., Nikola T., Parshley S. C., Benford D. J., Staguhn J. G., Fiolet N., 2010, ApJ, 724, 957
Stutzki J., Stacey G. J., Genzel R., Harris A. I., Jaffe D. T., Lugten J. B., 1988, ApJ, 332, 379
Swinbank A. M. et al., 2010, Nature, 464, 733
Swinbank A. M. et al., 2011, ApJ, 742, 11
Swinbank A. M., Smail I., Sobral D., Theuns T., Best P. N., Geach J. E., 2012, ApJ, 760, 130
Tacconi L. J. et al., 2010, Nature, 463, 781
Valtchanov I. et al., 2011, MNRAS, 415, 3473
Venemans B. P. et al., 2012, ApJ, 751, L25
Vieira J. D. et al., 2010, ApJ, 719, 763
Vieira J. D. et al., 2013, Nature, 495, 344
Viti S., Bayet E., Hartquist T. W., Bell T. A., Williams D. A., Banerji M., 2013, in Torres D. F., Reimer O., eds, Astrophysics and Space Science Proc., Vol. 34, Cosmic Rays in Star-Forming Environments. Springer-Verlag, Berlin, p. 7
Wagg J., Carilli C. L., Wilner D. J., Cox P., De Breuck C., Menten K., Riechers D. A., Walter F., 2010, A&A, 519, L1
Wagg J. et al., 2012, ApJ, 752, L30
Walter F. et al., 2012, Nature, 486, 233
Wang R. et al., 2013, ApJ, 773, 44
Weiß A. et al., 2013, ApJ, 767, 88
Willott C. J., Omont A., Bergeron J., 2013, ApJ, 770, 13
Wolfire M. G., Hollenbach D., Tielens A. G. G. M., 1989, ApJ, 344, 770
Wolfire M. G., Tielens A. G. G. M., Hollenbach D., 1990, ApJ, 358, 116
Wolfire M. G., Hollenbach D., Tielens A. G. G. M., 1993, ApJ, 402, 195
Young J. S. et al., 1995, ApJS, 98, 219

APPENDIX A: NEW REDSHIFTS

All but two sources observed in [C II] were published by Weiß et al. (2013), where the full source names are listed. The two new sources were selected from the list of Mocanu et al. (2013), and observed as part of our ongoing ALMA Cycle 1 project to determine redshifts of additional SPT DSFGs. Table A1 lists their full names and ALMA band 3 continuum positions. The redshift of SPT2319-55 is based on detections of CO(5–4) and CO(6–5), while the redshift of SPT2311-54 is based on CO(5–4) confirmed by our APEX [C II] detection (Fig. 1).

Table A1. Source names are based on positions measured with the SPT (Mocanu et al. 2013). Source positions are based on the ALMA 3-mm continuum data.

Short name	Source	R.A.	Dec.
		J2000	
SPT2311-54	SPT-S J231124-5450.5	23:11:23.94	−54:50:30.0
SPT2319-55	SPT-S J231922-5557.9	23:19:21.67	−55:57:57.8

APPENDIX B: HIGH-z COMPARISON GALAXIES

Table B1. The high-z sources in the comparison sample. All but one sources (ALESS61.1) have published [C II] and CO detections. The observed CO luminosities have been scaled to CO(1–0) luminosities using the ratios from Stacey et al. (2010). The first 14 sources have a sufficient amount of photometric data published for the determination of $L_{\rm FIR}$ and $T_{\rm d}$, while the remaining are unconstrained. ALESS61.1 has good photometry, but no published low-J CO observations. ⋆A sum of the [CII] and CO emission from the north and south source. †AGN-dominated source.

Source	z	$L_{[C\,II]}$ (10^9 $L_\odot$)	$L_{CO(1-0)}$ (10^6 $L_\odot$)	$L_{\rm FIR}$ (10^{12} $L_\odot$)	$T_{\rm d}$ (K)	Lensing magnification	[C II] and CO reference
SMMJ2135−0102 (Eyelash)	2.33	5.8 ± 1.3	0.8 ± 0.04	40.9 ± 9.1	36.0 ± 2.3	32.5 ± 4.5	Swinbank et al. 2010; Ivison et al. 2010
SDP.130	2.63	<65	10.1 ± 2.9	17.5 ± 3.6	38.6 ± 2.0	6 ± 1	Valtchanov et al. 2011; Frayer et al. 2011
SDP.81	3.04	275 ± 39	22.0 ± 5.0	33.1 ± 6.3	40.0 ± 1.8	25 ± 7	Valtchanov et al. 2011; Frayer et al. 2011
PSSJ2322+1944†	4.12	<8.0	6.1 ± 2.6	28.6 ± 10.2	55.8 ± 6.1	5.4 ± 0.3	Benford et al. in prep., Carilli et al. 2002b
SDP.141	4.24	60 ± 9	38.7 ± 4.6	66.2 ± 17.7	46.1 ± 3.2	10 − 30	Cox et al. 2011
BRI1335−0417†	4.41	15.7 ± 2.5	4.4 ± 0.8	17.7 ± 4.9	51.3 ± 4.4	–	Wagg et al. 2010; Carilli et al. 2002a
ALESS65.1	4.45	3.2 ± 0.4	<1.11	3.12 ± 1.40	44.3 ± 5.1	–	Swinbank et al. 2012; Huynh et al. 2014
BR1202−0725⋆†	4.69	15.8 ± 1.8	5.4 ± 0.7	34.1 ± 8.4	55.1 ± 4.3	–	Wagg et al. 2012; Carilli et al. 2002a
HDF850.1	5.19	7.5 ± 0.8	2.2 ± 0.5	1.7 ± 1.6	29.9 ± 7.7	1.5 − 1.7	Neri et al. 2014; Walter et al. 2012
HLSJ091828.6+514223	5.24	82.4 ± 2.3	43.0 ± 3.3	97.5 ± 24.4	48.7 ± 3.0	8.9 ± 1.9	Rawle et al. 2014
SDSSJ1044−0125†	5.78	1.6 ± 0.4	1.6 ± 0.3	5.6 ± 5.1	59.8 ± 25.8	–	Wang et al. 2013
SDSSJ2310+1855†	6.00	8.7 ± 1.4	12.1 ± 1.0	20.0 ± 14.5	61.8 ± 20.7	–	Wang et al. 2013
HerMESFLS3	6.34	14.9 ± 3.1	4.6 ± 1.5	29.9 ± 9.6	52.8 ± 6.2	2.2 ± 0.3	Riechers et al. 2013
SDSSJ1148+5251†	6.42	4.6 ± 0.5	6.4 ± 0.7	9.8 ± 6.7	60.9 ± 15.7	–	Maiolino et al. 2005
IRASF10026+4949	1.12	25.8 ± 3.2	<0.8	–	–	–	Stacey et al. 2010
3C368	1.13	9.3 ± 1.5	<1.9	–	–	–	Stacey et al. 2010; Evans et al. 1996
SMMJ123634.51+621241.0	1.22	14.4 ± 2.0	3.76 ± 0.12	–	–	–	Stacey et al. 2010; Frayer et al. 2008
MIPSJ142824.0+352619	1.32	10.5 ± 3.1	1.10 ± 0.03	–	–	–	Hailey-Dunsheath et al. 2010; Iono et al. 2006
SDSSJ100038.01+020822.4†	1.83	10.6 ± 2.4	3.10 ± 0.17	–	–	–	Stacey et al. 2010; Aravena et al. 2008
SWIREJ104704.97+592332.3	1.95	20.0 ± 2.6	8.9	–	–	–	Stacey et al. 2010
SWIREJ104738.32+591010.0	1.96	12.1 ± 3.2	3.5	–	–	–	Stacey et al. 2010
BRI0952−0115†	4.44	4.5 ± 2.6	0.43 ± 0.11	–	–	–	Maiolino et al. 2009; Guilloteau et al. 1999
LESSJ033229.4−275619†	4.76	9.9 ± 1.5	1.05 ± 0.25	–	–	–	De Breuck et al. 2011; Coppin et al. 2010
SDSSJ0129−0035†	5.78	1.8 ± 0.3	2.8 ± 0.5	–	–	–	Wang et al. 2013
SDSSJ2054−0005†	6.04	3.3 ± 0.5	2.7 ± 0.6	–	–	–	Wang et al. 2013
ULASJ1319+0950†	6.13	4.4 ± 0.9	3.5 ± 0.7	–	–	–	Wang et al. 2013
CFHQSJ0210−0456†	6.43	0.30 ± 0.04	<0.88	–	–	–	Willott, Omont & Bergeron 2013
ALESS61.1	4.42	1.48 ± 0.23	–	3.0 ± 1.4	43.7 ± 5.1	–	Swinbank et al. 2012

[1]*European Southern Observatory, Karl Schwarzschild Straße 2, D-85748 Garching, Germany*
[2]*Department of Astronomy and Department of Physics, University of Illinois, 1002 West Green Street, Urbana, IL 61801, USA*
[3]*Max-Planck-Institut für Radioastronomie, Auf dem Hügel 69, D-53121 Bonn, Germany*
[4]*University of Pennsylvania, 209 South 33rd Street, Philadelphia, PA 19104, USA*
[5]*European Southern Observatory, Alonso de Cordova 3107, Casilla 19001, Vitacura, Santiago, Chile.*
[6]*Núcleo de Astronomía, Facultad de Ingeniería, Universidad Diego Portales, Av. Ejército 441, Santiago, Chile*
[7]*Jet Propulsion Laboratory, 4800 Oak Grove Drive, Pasadena, CA 91109, USA*
[8]*Cavendish Laboratory, University of Cambridge, JJ Thompson Ave, Cambridge CB3 0HA, UK*
[9]*Kavli Institute for Cosmological Physics, University of Chicago, 5640 South Ellis Avenue, Chicago, IL 60637, USA*
[10]*Enrico Fermi Institute, University of Chicago, 5640 South Ellis Avenue, Chicago, IL 60637, USA*
[11]*Department of Physics, University of Chicago, 5640 South Ellis Avenue, Chicago, IL 60637, USA*
[12]*Department of Astronomy and Astrophysics, University of Chicago, 5640 South Ellis Avenue, Chicago, IL 60637, USA*
[13]*Dalhousie University, Halifax, Nova Scotia B3H 4R2, Canada*
[14]*Department of Physics, University of California, One Shields Avenue, Davis, CA 95616, USA*
[15]*Department of Astronomy, University of Florida, Gainesville, FL 32611, USA*
[16]*Department of Physics and Astronomy, University College London, Gower Street, London WC1E 6BT, UK*
[17]*Kavli Institute for Particle Astrophysics and Cosmology, Stanford University, Stanford, CA 94305, USA*
[18]*Department of Physics, University of California, Berkeley, CA 94720, USA*
[19]*H.H. Wills Physics Laboratory, University of Bristol, Tyndall Avenue, Bristol BS8 1TL, UK*
[20]*Department of Physics and Astronomy, University of California, Los Angeles, CA 90095-1547, USA*
[21]*Steward Observatory, University of Arizona, 933 North Cherry Avenue, Tucson, AZ 85721, USA*
[22]*Infrared Processing and Analysis Center, California Institute of Technology, MC 220-6, Pasadena, CA 91125, USA*
[23]*Harvard–Smithsonian Center for Astrophysics, 60 Garden Street, Cambridge, MA 02138, USA*
[24]*Department of Physics, Oxford University, Denis Wilkinson Building, Keble Road, Oxford OX1 3RH, UK*

This paper has been typeset from a TEX/LATEX file prepared by the author.